The evolution of galaxy shapes in CANDELS: from prolate to discy

Haowen Zhang [1,2]★ Joel R. Primack,[3,4] S. M. Faber,[5] David C. Koo,[5]
Avishai Dekel,[4,6] Zhu Chen,[7] Daniel Ceverino,[8] Yu-Yen Chang,[9] Jerome J. Fang,[10]
Yicheng Guo,[11] Lin Lin[12] and Arjen van der Wel[13,14]

[1]*The School of Physics, Peking University, Peking University, Beijing 100871, China*
[2]*Kavli Institute of Astronomy and Astrophysics, Peking University, Peking University, Beijing 100871, China*
[3]*Physics Department, University of California, Santa Cruz, CA 95064, USA*
[4]*SCIPP, University of California, Santa Cruz, CA 95064, USA*
[5]*UCO/Lick Observatory, Department of Astronomy and Astrophysics, University of California, Santa Cruz, CA 95064, USA*
[6]*Racah Institute of Physics, The Hebrew University, Jerusalem 91904, Israel*
[7]*Mathematics and Science College of Shanghai Normal University, Shanghai 200234, China*
[8]*Institut für Theoretische Astrophysik, Zentrum für Astronomie der Universität, D-69120 Heidelberg, Germany*
[9]*Academia Sinica Institute of Astronomy and Astrophysics, PO Box 23-141, Taipei 10617, Taiwan*
[10]*Orange Coast College, Costa Mesa, CA 92626, USA*
[11]*Department of Physics and Astronomy, University of Missouri, Columbia, MO 65211-7010, USA*
[12]*Shanghai Astronomical Observatory, Shanghai 200030, China*
[13]*Sterrenkundig Observatorium, Universiteit Gent, Krijgslaan 281 S9, B-9000 Gent, Belgium*
[14]*Max-Planck Institut für Astronomie, Königstuhl 17, D-69117 Heidelberg, Germany*

ABSTRACT

We model the projected b/a–$\log a$ distributions of CANDELS star-forming main-sequence galaxies, where a (b) is the half-light semimajor (semiminor) axis of the galaxy images measured by GALFIT. We find that smaller a galaxies are rounder at all stellar masses M_* and redshifts, so we include a when analysing b/a distributions. Approximating intrinsic shapes of the galaxies as triaxial ellipsoids and assuming a multivariate normal distribution of galaxy size and two shape parameters, we construct their intrinsic shape and size distributions to obtain the fractions of elongated (prolate), discy (oblate), and spheroidal galaxies in each redshift and mass bin. We find that galaxies tend to be prolate at low M_* and high redshifts, and discy at high M_* and low redshifts, qualitatively consistent with van der Wel et al., implying that galaxies tend to evolve from prolate to discy. These results are consistent with the predictions from simulations that the transition from prolate to oblate is caused by a compaction event at a characteristic mass range, making the galaxy centre baryon dominated. We give probabilities of a galaxy's being elongated, discy, or spheroidal as a function of its M_*, redshift, and projected b/a and a, which can facilitate target selections of galaxies with specific shapes at high redshifts.

Key words: galaxies: evolution – galaxies: formation – galaxies: fundamental parameters.

1 INTRODUCTION

The shape of a galaxy's stellar component is closely related to the formation and evolution of the galaxy. Although the effect of viewing orientations plays some role, the evolution of the projected shapes of galaxies reflect that of their intrinsic shapes. Elmegreen et al. (2005) found that the projected ellipticity distribution of the spiral galaxies in the Hubble Ultra Deep Field peaks (HUDF) at ∼0.55, indicating thicker discs by a factor of ∼2 than the local

disc galaxies. Similar findings have been made on the Lyman Break Galaxies (LBGs) in the Great Observatories Origins Deep Survey (GOODS) by Ravindranath et al. (2006), which finds an evolution of the peak of the projected ellipticity from ∼0.7 at $z = 4$ to ∼0.5 at $z = 3$. Later works went further by modelling the intrinsic shape distributions of galaxies using the projected b/a axial ratio distributions. By assuming that the shapes of ellipticals and spirals can be well approximated by triaxial ellipsoids, Padilla & Strauss (2008) modelled the intrinsic shape distribution of a subset of SDSS galaxies, and found that generally brighter (and more massive) galaxies tend to be rounder. They also found that the intrinsic shapes
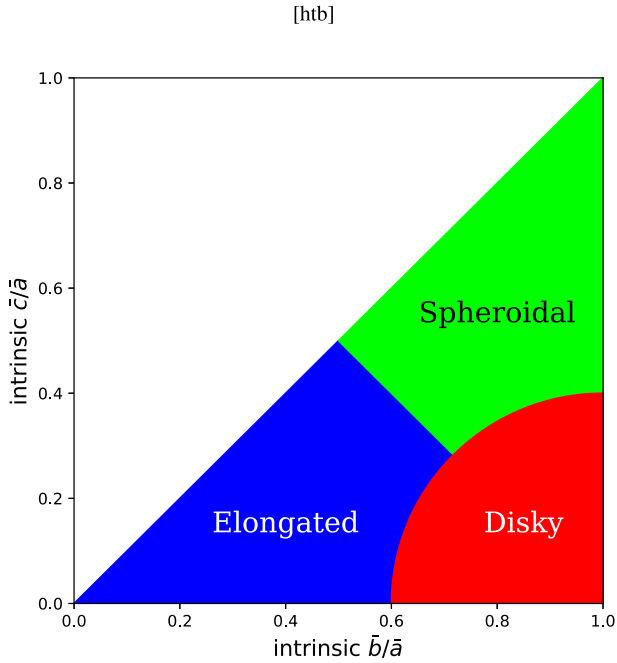
★ E-mail: hwzhang0595@email.arizona.edu

[htb]

Figure 1. The definition of the three shapes of galaxies used by van der Wel et al. (2014). Note that under such definitions, a spheroidal galaxy could be quite triaxial, so we recommend to rename the 'spheroidal' galaxies as 'spheroidal or triaxial' objects. Such definitions are certainly not unique, which we choose to follow mainly for the sake of the direct comparison between our results and those from van der Wel et al. (2014).

of the galaxies are correlated with their sizes in the sense that the median b/a decreases as one looks at the galaxies with larger a.

Based on similar modelling methodology, Law et al. (2012) found that the intrinsic shapes of the star-forming galaxies in the *HST*/WFC3 survey with $1.5 < z < 3.6$ are more consistent with a triaxial population, with intrinsic $b/a \sim 0.7$ and $c/a \sim 0.3$, rather than thick oblate discs despite the galaxies mostly having exponential surface brightness profiles (Sérsic index $n \sim 1$). van der Wel et al. (2014) determined the intrinsic shape distributions of star-forming galaxies with $0 < z < 2.5$ from SDSS and Cosmic Assembly Near-Infrared Deep Extragalactic Legacy Survey (CANDELS). The basic assumption was that the galaxies are triaxial ellipsoids with intrinsic axis lengths $\bar{a} \geq \bar{b} \geq \bar{c}$ with a Gaussian distribution of the ellipticity ($E = 1 - \bar{c}/\bar{a}$) and triaxiality ($T = \left(\bar{a}^2 - \bar{b}^2\right) / \left(\bar{a}^2 - \bar{c}^2\right)$). Fig. 1 shows the definition of three different galaxy shapes (i.e. discy, elongated, and spheroidal) used by van der Wel et al. (2014). Note that, although technically defined as spheroidal, some galaxies can have quite small apparent b/a because of an allowed intrinsic $\bar{c}/\bar{a}$ as small as 0.3. Thus actually we recommend that one rename the 'spheroidal' galaxies defined by Fig. 1 as 'spheroidal or triaxial'. Such a definition on the shape of galaxies is by no means unique, but we choose to follow it mainly for the sake of the comparison between this work and van der Wel et al. (2014). Another pair of closely related concepts of galaxy shape is 'prolate' and 'oblate', meaning that a galaxy's intrinsic shape satisfies $\bar{b} \sim \bar{c} < \bar{a}$ or $\bar{b} \sim \bar{a} > \bar{c}$, which is covered by our definition of 'elongated' and 'discy' shape, respectively. Throughout this work we will use 'elongated' and 'discy' as definitions of galaxy shapes, but will describe galaxies as prolate or oblate when it is more accurate to do so. By finding the best-fitting parameters that describe such Gaussian distributions, van der Wel et al. (2014) found that the fraction of elongated galaxies decreases with increasing time and

mass. At high redshift, they found that low-mass galaxies are a mixture of roughly equal numbers of elongated and discy galaxies, while the fraction of elongated galaxies remains negligible for the most massive populations throughout the whole redshift range. Qualitatively the picture indicated by their results is that the overall oblateness (i.e. the fractions of discy objects) of galaxies increases with time, and that this process proceeds earlier in higher mass galaxies. Recently, Jiang et al. (2018) analysed the radial profiles of the isophotal ellipticity $\epsilon = 1 - b/a$ and discy/boxy parameter A_4 of $\sim$4600 star-forming galaxies (SFGs) within CANDELS with $9.0 < \log\left(M_*/M_\odot\right) < 11.0$ and $0.5 < z < 1.8$. By dividing the whole sample into a series of redshift-mass bins, they found that the more massive galaxies in lower redshifts have more discy isophotes at intermediate radii, which is consistent with the picture indicated by the findings of van der Wel et al. (2014). By further dividing the sample into large and small SFGs using the deviation from the size–mass relation in each redshift bin, they also found that larger SFGs typically have isophotes with larger ϵ (i.e. more elongated) when compared with small SFGs.

The evolution of galaxy shapes has also been investigated from a theoretical perspective. A shape evolution from prolate to oblate in three dimensions has been revealed and studied in the VELA zoom-in cosmological simulations (Ceverino, Primack & Dekel 2015; Tomassetti et al. 2016). In the simulations, the galaxies tend to experience an early-prolate phase while their interiors (radii lower than the galaxy half-mass radius) are dominated by dark matter. They thus follow the prolateness of the inner dark matter halo, generated by mergers along a cosmic-web filament and being supported by anisotropic velocity dispersion (Allgood et al. 2006). After a major wet compaction event in which inflowing gas makes the galaxy compact and baryon dominated, the stellar orbits supporting the prolateness are deflected and the system evolves into an oblate shape, induced by the angular momentum of the newly accreted mass. The major compaction events (defined as the moment at which the amount of the baryonic mass in the central 1 kpc sphere exceeds that of the dark matter in the same aperture) tend to occur in a characteristic mass range, $M_* \sim 10^{9.5-10}\,M_\odot$ (Zolotov et al. 2015; Tomassetti et al. 2016; Tacchella et al. 2016a; Tacchella et al. 2016b). Therefore, more massive galaxies at a given redshift are predicted to make the transition from prolate to oblate at a higher redshift. One can test these predictions using the projected shapes of a large observed sample of galaxies.

There exists a potential problem with several of the previous observational analyses, which were based on the projected b/a distribution only: as Padilla & Strauss (2008) pointed out, the projected and intrinsic shapes of SDSS galaxies are correlated with their R_e (hereafter a). Similarly, Fang (2015) and Fang et al. (2018) found that the projected shapes of the CANDELS galaxies are correlated with their residuals from the $\log a$–$\log M_*$ relation, which serves as another indicator of galaxy sizes. Given this fact, one should in principle carry out such b/a modellings on galaxy subsamples in different a bins as Padilla & Strauss (2008) did to avoid potential bias in the fractions of the galaxies with different shapes. Alternatively one can also directly model the two-dimensional projected b/a–$\log a$ distribution and overcome this potential bias by allowing correlation between intrinsic shape parameters and sizes. In this work we try to make such two-dimensional modellings to better determine the fractions of star-forming galaxies with different shapes at a given mass and redshift, and to further test the picture that the oblateness (prolateness) of star-forming galaxies increases (decreases) with increasing time and mass, which is expected, if the prediction made by Ceverino et al. (2015) and Tomassetti et al. (2016) is true, that

there is a characteristic mass range where the galaxies go through a shape transition.

This paper is organized as follows. In Section 2, we describe our criteria for data selection, and give some visual impressions of the distributions of the data in the projected b/a–$\log a$ plane. Section 3 describes our methodology to model such a two-dimensional distribution. The modelling results are shown in Section 4. In Section 5 we give some further discussions based on our modelling results. Section 6 lists several caveats regarding the analysis in this work. In Section 7 we summarize our results. Appendices discuss tests of potential selection effects in the CANDELS pipeline and provide further discussions of our modelling of galaxy shapes.

Throughout this paper we use *AB* magnitudes and adopt the cosmological parameters $(\Omega_M, \Omega_\Lambda, h) = (0.3, 0.7, 0.7)$. To differentiate projected and intrinsic lengths, we denote the projected ones as $(a, b, b/a)$ and the intrinsic ones as $(\bar{a}, \bar{b}, \bar{c})$, etc..

2 DATA

This work makes use of the multiwavelength and ancillary data sets produced by the CANDELS (Grogin et al. 2011; Koekemoer et al. 2011). The data reduction and cataloguing for each of the fields is presented in Nayyeri et al. (2017, COSMOS), Stefanon et al. (2017, EGS), Barro et al. (in preparation, GOODS-N), Guo et al. (2013); Santini et al. (2015, GOODS-S) and Galametz et al. (2013); Santini et al. (2015, UDS). The GALFIT measurements of the b/a and a of CANDELS galaxies used in this work are obtained by van der Wel et al. (2012).[1]

2.1 Data selection

For the sake of a direct comparison between this work and van der Wel et al. (2014), it would have been best to model the same data that they used. But van der Wel et al. (2014) used the UVJ diagram (Wuyts et al. 2007; Williams et al. 2009) method to pick out star-forming galaxies, which tends to include green valley galaxies. Also, their sample is highly incomplete in the $2.0 < z < 2.5$ and $9.0 < \log(M_*/M_\odot) < 9.5$ bin. Thus in addition to the galaxies used in van der Wel et al. (2014), we also pick out just the star-forming main-sequence (SFMS) galaxies in CANDELS data, which is a complete sample in all the redshift and mass bins we study. Since this different sample selection does not change the main conclusions of this work, we will only show the results based on the SFMS galaxies in CANDELS. Our selection criteria for SFMS galaxies are based on the deviation from the SFMS defined by specific star formation rates (ΔSSFR) in each redshift-mass bin following the same method and formulae of Fang et al. (2018). The SSFR-mass main sequence in each redshift bin is defined as (Fang et al. 2018):

$$\langle \log \text{SSFR} \rangle = c_1 (\log M_* - 10) + c_2 \tag{1}$$

where the parameters c_1 and c_2 are determined in the linear fitting. Based on ΔSSFR, our selection criteria are:

(1) $H_{\text{F160W}} < 25.5$;
(2) $z < 2.5$;
(3) $M_* > 10^9 \, M_\odot$;
(4) ΔSSFR > -0.45 dex;
(5) have good GALFIT measurements of the structural parameters.

---

[1] All of the data used in this work can be accessed from the *Rainbow* data base (Barro et al. 2011), whose URL is http://arcoiris.ucsc.edu//Rainbow_navigator_public/. All the GALFIT output files can be found at http://www.mpia.de/homes/vdwel/3dhstcandels.html.

The data used in our modelling are the projected axial ratio b/a and projected semimajor axis a of the observed galaxies. These structural parameters are measured by GALFIT (Peng et al. 2010), and the GALFIT set-up can be found in van der Wel et al. (2012). To have the galaxies' shapes measured at a rest-frame wavelength as close as possible to 4600 Å in order to avoid the effect that the shape of a galaxy changes with wavelength, which is seen in local galaxies (Dalcanton & Bernstein 2002), we use the structural parameters measured from *H*-band (F160W) images for $2 < z < 2.5$ galaxies and the ones measured from *J*-band (F125W) images for those with $z < 2$.

The lowest redshift bins ($0 < z < 0.5$) and the most massive bins ($10.5 < \log(M_*/M_\odot) < 11.0$) in van der Wel et al. (2014) are excluded from the quantitative modelling because our two-dimensional binning process requires a minimum sample size, and the numbers of the galaxies in such bins are too small to be modelled robustly. But we will still give some qualitative comments on the general trends with redshift shown in the most massive bins. Note that the numbers and the histograms in fig. 1 of van der Wel et al. (2014) do not match each other: the numbers in the first row correspond to the histograms in the second row, and vice versa. We refer the readers to van der Wel et al. (2012) for more information on the determination of the measurement uncertainties of the structural parameters.

2.2 Visual impressions of the data

Fig. 2 shows the projected b/a–$\log a$ scatter plot for galaxies in each bins of mass and redshift, colour coded by their A_V values. Note that galaxies evolve with redshift diagonally upwards and to the right in this diagram (Fang et al. 2018, Fig. 5). There are some noteworthy features in these plots. First a curved boundary at the lower left corner of each panel is clearly seen, which is qualitatively compatible with a population of galaxies with a constant or slowly evolving intrinsic shortest main axis. Secondly there is a lack of objects at the upper right corner of each panel at higher redshifts, increasingly filled with galaxies as the redshift decreases and the mass increases. We will give a more extended discussion of this trend with redshift and mass in Section 4.1. But we emphasize that these two features are not induced by the selection effects in the detection and measurement pipeline. To demonstrate this, we carried out a two-step experiment, each step of which mocks the process of detections and measurements in the pipeline, respectively. See the Appendix for a description of the assumptions, implementation, and results of such an experiment. Given the visual impressions of the b/a–$\log a$ distributions of the galaxies, one can be convinced that the assumption of van der Wel et al. (2014) that the intrinsic shapes of galaxies are independent of their sizes is in fact not the case. The implications of the A_V distributions are discussed in Section 4.

Fig. 3 shows the projected $\log b$–$\log a$ distributions of the galaxies with different masses and redshifts, again colour coded by A_V values. We can see that in most panels the lower boundary of the distribution can be fitted pretty well by a straight line, which may imply relations between the intrinsic $\bar{c}$ and $\bar{a}$. This changing lower boundary with $\log a$ serves as further supporting evidence that the curved boundary giving the smallest b/a is not an artificial result of the instrumental resolutions, because if the opposite were the case, the lowest observed $\log b$ would be constant over the whole range of $\log a$.

Fig. 4 compares histograms of b/a of galaxies with different sizes in each redshift-mass bin. Since galaxies grow in size with
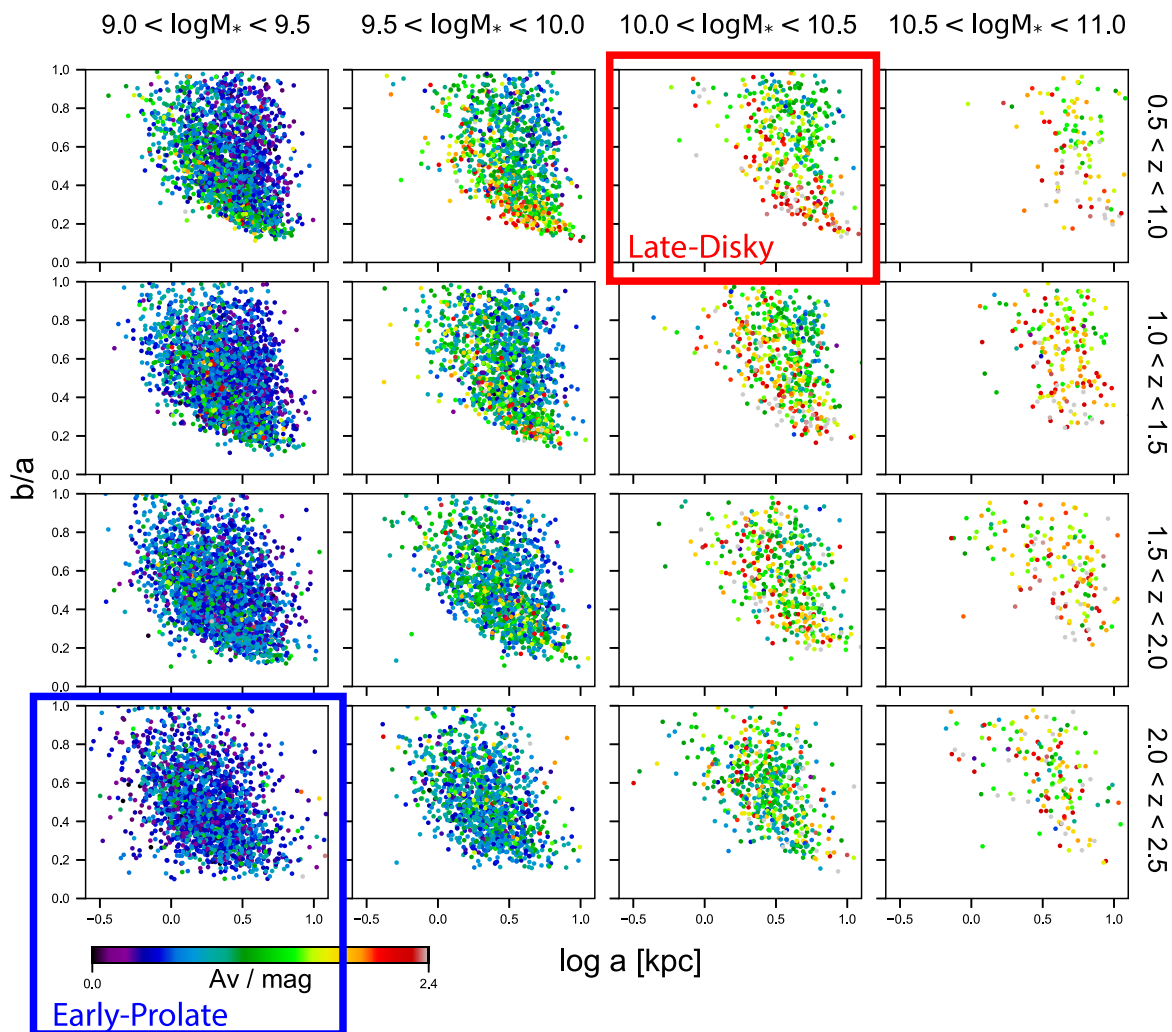
Figure 2. The projected *b/a*–log *a* distributions of CANDELS galaxies in all the redshift-mass bins. Here stellar mass M_* is in units of M$_\odot$, and the points are colour coded by attenuation A_V values from SED fitting. Note the strong trend of smaller galaxies being rounder and the increasing number of galaxies in the upper right corner of the panels with increasing time and mass. In the following quantitative analysis of the galaxy shapes we found that most galaxies with $2.0 < z < 2.5$ and $9 < \log(M_*/M_\odot) < 9.5$ ($0.5 < z < 1.0$ and $10 < \log(M_*/M_\odot) < 10.5$) are prolate and discy, respectively (see Fig. 12), so we call these two bins as 'early-prolate' and 'late-discy', respectively, and emphasize them with blue and red squares. These two bins are also emphasized in Figs 3, 4, and 12.

time and mass, we cancel out this systematic effect by fitting the size–mass relation in each redshift bin and use the residuals from these relations (i.e. $\Delta \log a$) as a measure of the size of the galaxies. For the fitting results see Fang et al. (2018). The blue and red open histograms show the (normalized) *b/a* of distributions galaxies in slices of small $\Delta \log a$ and large $\Delta \log a$, respectively. The orange one shows distributions of all the galaxies in that redshift bin. We see first that the *b/a* distributions of small and large galaxies are quite different in that the smaller objects (blue lines) tend to be clustered at larger *b/a* values and therefore are intrinsically rounder, while the *b/a* distributions of the larger galaxies (red lines) peak at a smaller value and have long tails, which implies that these objects are more likely to be elongated or discy galaxies instead of spheroids. Thus if one simply models the single marginalized *b/a* distribution, one may end up mistaking both small spheroidal galaxies and large elongated ones for discy objects, since such a marginalization over the log *a* dimension tends to give a flatter global *b/a* distribution (which favours more discy galaxies) than the ones where only the galaxies of a certain size are involved. To overcome this danger of modelling the marginalized

b/a distribution is the main motivation for this work, where the correlations between the size and the shape of galaxies are included simultaneously.

2.3 Mock images from the VELA simulations

Besides the data from observations, we also make use of the mock images generated from the VELA set of high-resolution hydrodynamic cosmological zoom-in galaxy simulations (Ceverino et al. 2014; Ceverino et al. 2015; Snyder et al. 2015; Zolotov et al. 2015; Tacchella et al. 2016a; Tacchella et al. 2016b, and references cited there). The images are produced by SUNRISE, which is a parallel Monte Carlo code for the calculation of radiation transfer (Jonsson 2006; Jonsson & Primack 2010; Jonsson, Groves & Cox 2010). In the generation of such mock images, emission lines, the effects of stellar evolution, scattering and absorption by dust, the resolution of the instrument (i.e. *HST*/WFC3), the point spread function (PSF), and sky background are included. We use GALFIT (Peng et al. 2010) to measure the structural parameters of all the *J*-band (F125W) mock images of the galaxies with $1 < z < 2$ and the *H*-band (F160W)
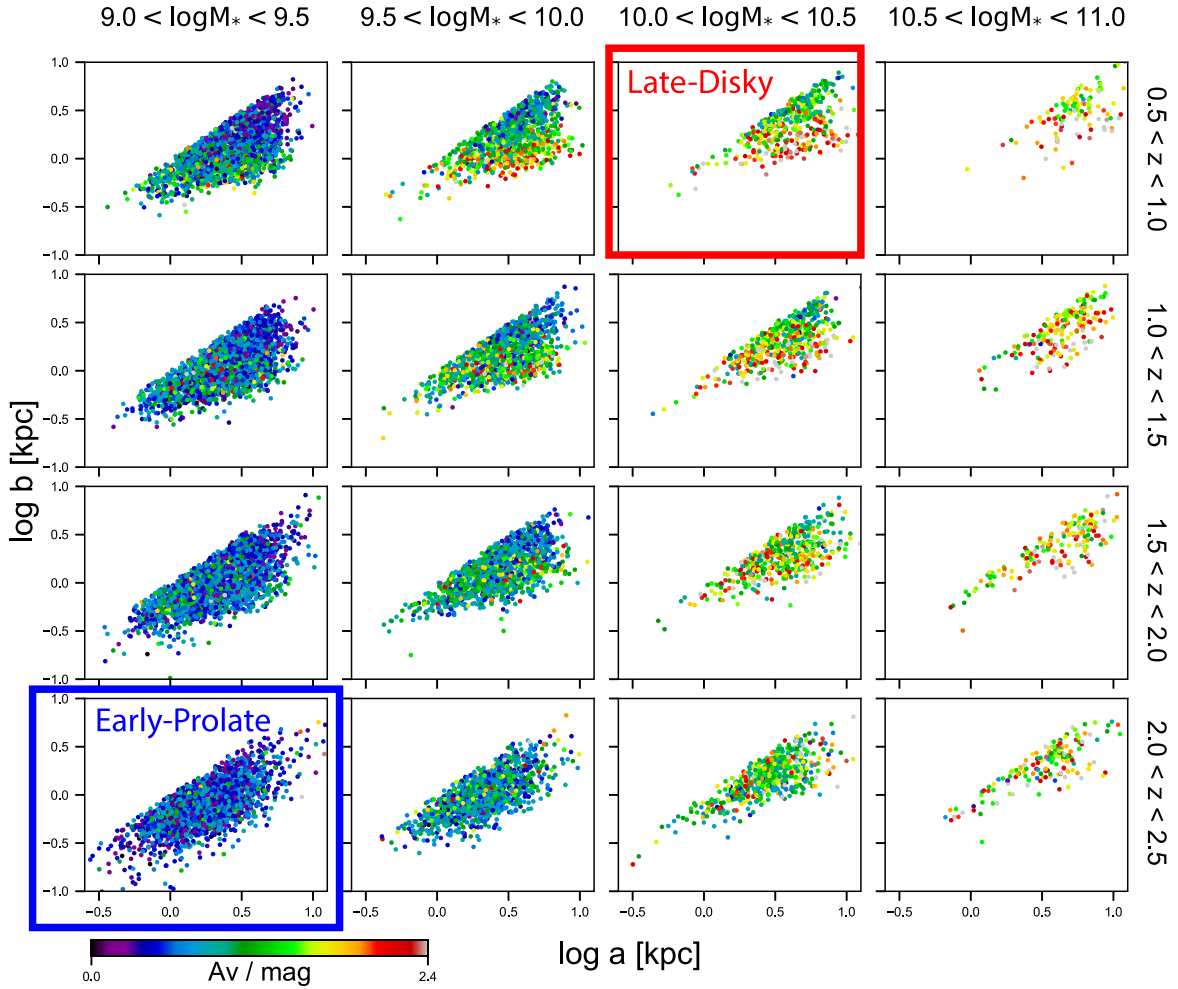
Figure 3. log b–log a distributions of the galaxies in all the redshift-mass bins, colour coded by A_V values from SED fitting. The early-prolate bin and late-discy bin, as defined in the caption of Fig. 2 and Section 3.2, are squared in blue and red, respectively.

images of the ones with $2 < z < 3$. By doing this we get ~6500 good[2] GALFIT measurements for the images of 34 VELA galaxies from multiple orientation at a series of time-steps. The reason why we choose this redshift range is that for most of the VELA galaxies, the simulation only runs down to $z = 1$, while at redshifts higher than $z \sim 3$ the galaxies are too small (typically with $a \sim 1$ kpc at $3 < z < 4$) for GALFIT to measure the parameters robustly. The GALFIT set-up is identical to the one used in van der Wel et al. (2012). Note that for each galaxy at each time-step, mock images viewed from 19 different directions are made, of which seven are viewed from random directions from one time-step to the next. These images are qualitatively closest to the real observational data, and we call them the 'truly random' cameras.

3 MODELS

3.1 The model of individual galaxies

In our modelling of the two-dimensional b/a–log a distributions, a fundamental assumption is that a galaxy is modelled as a solid three-dimensional ellipsoid, with a set of intrinsic axes $(\bar{a}, \bar{b}, \bar{c})$,

which satisfy $\bar{a} \geq \bar{b} \geq \bar{c}$. The shape of a galaxy is completely determined by the two (intrinsic) axis ratios, $\bar{b}/\bar{a}$ and $\bar{c}/\bar{a}$. Our definitions of elongated, discy, and spheroidal galaxies are identical to the ones used in van der Wel et al. (2014) as shown in Fig. 1 in order to directly compare the results. When a galaxy is observed from a certain direction, specified by the polar angle θ and the azimuthal angle ϕ, the projected b/a and semimajor axis a can be calculated by measuring the shape and size of the projected two-dimensional ellipse. By projecting a galaxy randomly in the whole 4π solid angular space, one gets the theoretical projected b/a–log a probability distribution of the galaxy, which will serve as one of the building blocks for our models. To differentiate this solid ellipsoid modelling with the Sérsic model introduced in the Appendix, we call the former the 'ellipsoidal modelling'.

Fig. 5 shows the juxtaposition of the b/a–log a distributions of six such galaxies generated by the Sérsic modelling (left) and the ellipsoidal modelling (right), colour coded by the surface number density of points in their neighbourhoods. Before we go into the features of different kinds of galaxies, we point out that in the ellipsoidal modelling, we have taken into account the measurement uncertainties in both b/a and log a in the generation of these distributions by smearing them with an appropriate measurement uncertainty, which is adopted from van der Wel et al. (2012). In principle, the ellipsoidal model may be criticized for not being

[2] A measurement is good when all the fitting flags defined by van der Wel et al. (2012) are zero.
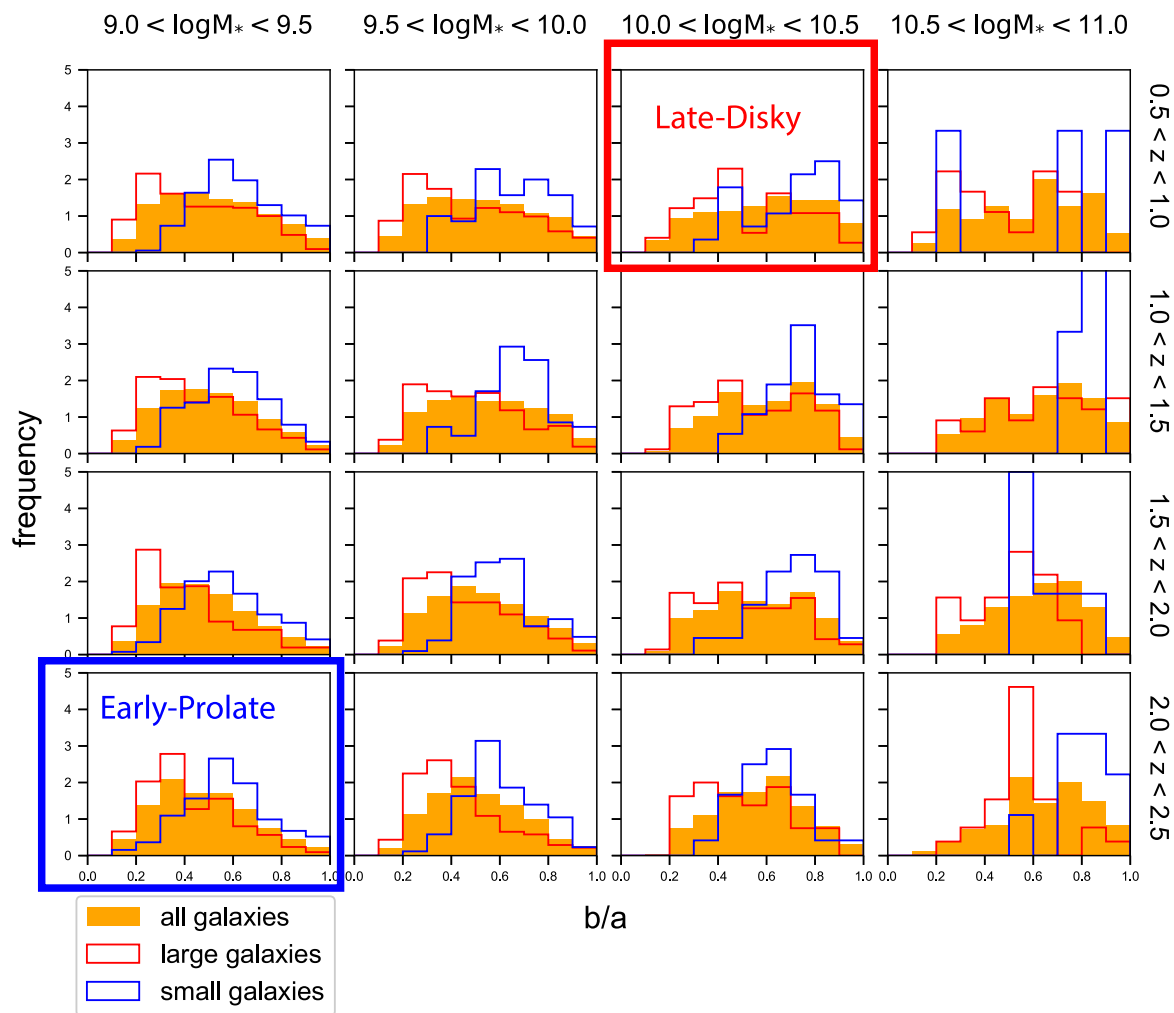
Figure 4. The normalized *b/a* histograms of galaxies of different sizes in all the redshift-mass bins. As galaxies grow in size with time, we use the residual in projected $\log a$ with respect to the star-forming galaxy size–mass relations at the corresponding redshift bin, $\Delta\log a$, as a measure of galaxy sizes in each redshift-mass bin. The size–mass relations used are obtained by Fang et al. (2018). Red open histogram: large galaxies with $0.15 < \Delta\log a < 0.25$, with a in kpc. Blue open histogram: small galaxies with $-0.35 < \Delta\log a < -0.25$. Orange filled histogram: all galaxies. Note how the blue histograms for small galaxies peak at systematically larger b/a values, indicating that small galaxies (at fixed mass and redshift) are intrinsically rounder. The early-prolate bin and late-discy bin, as defined in the caption of Fig. 2 and Section 3.2, are squared in blue and red, respectively.

realistic in the sense that it assumes the galaxies to have well-defined boundaries and are not transparent, which is not true. But from Fig. 5 it is clear that the *b/a*–$\log a$ distributions generated by the ellipsoidal modelling and the more realistic Sérsic modelling are similar in their shapes. Therefore we argue that the main conclusions in this work, which are made based on the ellipsoidal modelling, will not change qualitatively if we adopted this more realistic Sérsic modelling. Given the different magnitudes of scatter of the distributions, the exact best-fitting parameters and the fractions of different shapes may well change, though. For more discussion on the Sérsic modelling see the Appendix.

For discy galaxies (e.g. Figs 5a and b), the distributions are quite flat over a fairly large range of *b/a*. If a galaxy has perfectly round geometry when viewed face-on (i.e. intrinsic $\bar{b}/\bar{a} = 1$), theoretically we would observe a flat distribution all the way up to apparent $\bar{b}/\bar{a} = 1$. But due to the fact that random noise always causes the measured *b/a* to be an underestimate of the real one (Chang et al. 2013), a bump shows up at the relatively high *b/a* end owing to the fact that the definition of *b* and *a* are inverted. Another reason

for the existence of this bump is due to the intrinsic $\bar{b} < \bar{a}$. In this case, the probability that the projected galaxy has an apparent *b/a* that is close to the intrinsic one is larger, and thus there is a bump at the $(b/a) \sim (\bar{b}/\bar{a})$. On the other hand, due to the finite thickness of the disc, a second bump exists at the value around intrinsic $\bar{c}/\bar{a}$, which determines the value of the lowest projected *b/a*.

The distribution generated by an elongated galaxy is a curved trajectory (e.g. Figs 5c and d), and the shape of the curve depends on $(\bar{b}/\bar{a}, \bar{c}/\bar{a})$. Another noteworthy feature is that an elongated galaxy is much more likely to be viewed edge-on, which induces small projected *b/a* and large $\log a$. We can see this by simply appreciating how large the difference is between the number densities in the upper left and lower right corners in Fig. 5(c).

A triaxial galaxy (like Fig. 5e) can be regarded as an intermediate phase between elongated and discy objects, not only because the locus of such galaxies lies between the elongated and the discy regions in Fig. 1, but also because a typical triaxial galaxy (e.g. Fig. 5e) possesses features of both shapes: two bumps at lower and
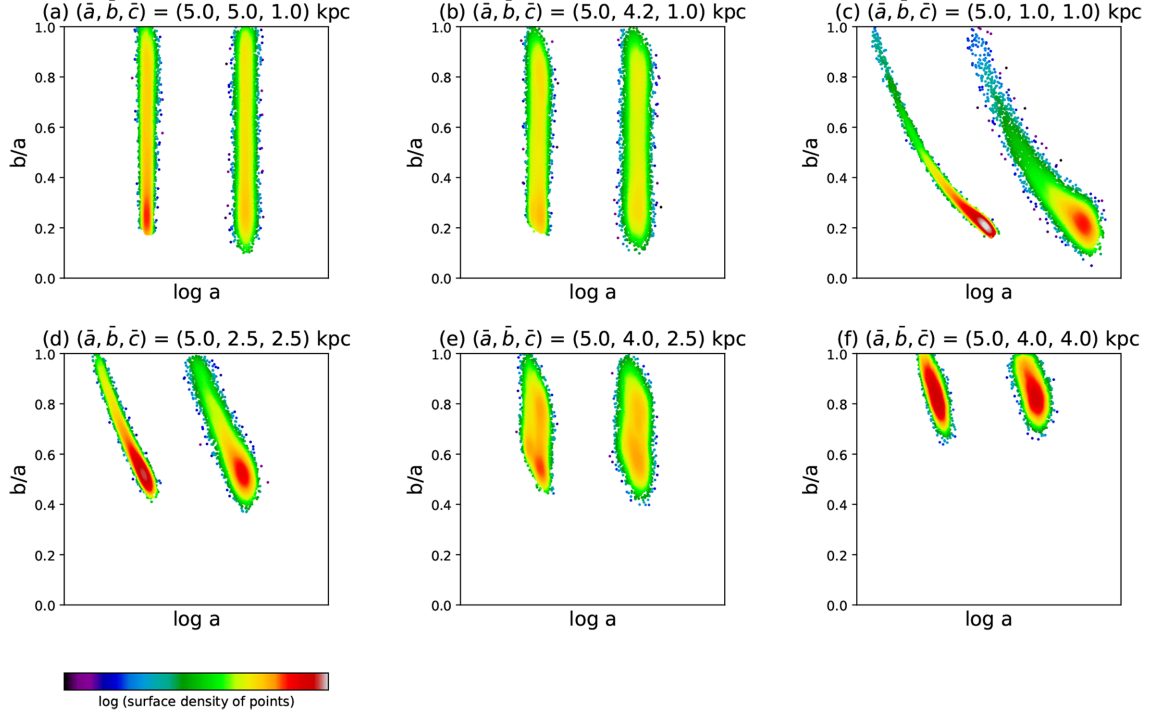
Figure 5. Comparison between b/a–$\log a$ distributions of galaxies with different shapes, generated in the Sérsic modelling, and those generated in the ellipsoidal modelling. The one in the left of each panel is from the Sérsic modelling, and the other one in the right is from the ellipsoidal modelling. They are offset to the left and right for clarity. The points are colour coded by the number density of the points in their neighbourhood. The distributions generated by the two models are qualitatively the same, although they have different magnitudes of scatters.

higher b/a ends, which is characteristic of a discy object, and a curved trend versus a, which is a feature of elongated galaxies.

For a spheroidal galaxy (Fig. 5f), the distribution is simply a small blob at large projected b/a, with less-complex internal structure than discy, elongated, or triaxial galaxies.

3.2 Empirical modelling of the b/a–$\log a$ distributions

From the visual inspections of the b/a–$\log a$ distributions of all the different redshift-mass bins in Fig. 2, we can see some features smoothly evolving with time and mass. This implies the possibility of fitting the distributions of all the bins using those of the two most extreme bins, with $0.5 < z < 1.0$ and $10 < \log(M_*/\mathrm{M}_\odot) < 10.5$ (squared in red in Figs 2, 3, 4, and 12, hereafter called the late-discy bin), and $2.0 < z < 2.5$ and $9 < \log(M_*/\mathrm{M}_\odot) < 9.5$ (squared in blue, hereafter called the early-prolate bin). We do such a simplified modelling to see whether it captures the picture, i.e. that the oblateness (prolateness) increases (decreases) with increasing time and mass. Specifically, we assume that the model b/a–$\log a$ distribution $P(b/a, \log a)$ in any redshift and mass bin is a linear combination of those of the two extreme bins, P_{prolate} and P_{discy}, both of which are normalized: $P_{\mathrm{model}}(b/a, \log a) = f \times P_{\mathrm{prolate}}(b/a, \log a) + (1 - f) \times P_{\mathrm{discy}}(b/a, \log a)$. To calculate the best-fitting weight of the early-prolate bin f, we renormalize $P_{\mathrm{model}}(b/a, \log a)$ so that it has the same normalization as the observed data, so that we can use the following formula to compute the log likelihood for the i-th b/a–$\log a$ bin: (Holden et al. 2012)

$$\log L_i = n_i \log(m_i) - m_i - \log(n_i!) \tag{2}$$

where n_i is the number of galaxies in this bin and m_i is the number predicted by the model. Given a further assumption that different

bins are independent of each other, the log of the total likelihood is simply a summation like

$$\log L = \sum_i \log L_i. \tag{3}$$

By using the Markov Chain Monte Carlo (MCMC) method we can find the best-fitting weight of the early-prolate bin f.

3.3 Fully quantative modelling of the b/a–$\log a$ distributions

Based on the prior knowledge that a more realistic model should involve the correlation between the size and the shape of galaxies, we extend the model in van der Wel et al. (2014) in this way: first we add a new dimension, $\log \bar{a}$, and model the two-dimensional distribution of the data on the b/a–$\log a$ plane; secondly our model population has a multivariate normal distribution of $(E, T, \gamma = \log \bar{a})$, with mean $(\bar{E}, \bar{T}, \bar{\gamma})$ and the covariance matrix Σ. Furthermore we allow only the covariance between E and γ, i.e. Cov$\langle E, \gamma \rangle$, to vary in the modelling, and both of the other two are set to zero. There are two reasons why we did not involve more covariances: First the existence of the curved boundary in the data distribution indicates the change of the intrinsic $\bar{c}/\bar{a}$ with the size of a galaxy, which can be most directly attributed to the covariance between $E = 1 - \bar{c}/\bar{a}$ and γ; and second, we have found that adding more covariance does not help to get a better modelling of the data in the sense that the likelihood calculated based on Poisson statistics does not improve. To differentiate this purely mathematical model from the empirical one introduced in Section 3.2, we call this model 'the ETa model'.

In principle the intrinsic shape parameter distributions may have a different form from the one described above (i.e. Multivariate

normal distribution). So we made some explorations on alternative models in the following two directions. The first is to assume that $(q = \bar{b}/\bar{a}, p = \bar{c}/\bar{b}, \log \bar{a})$, instead of $(E, T, \log \bar{a})$, has a multivariate normal distribution, and use the identical method to fit the data. The second one is to add more multivariate Gaussian populations of $(E, T, \log \bar{a})$. But we found that both of these alternative models produce more systematic residual patterns compared to the fiducial one. Therefore we finally chose stick to the fiducial model.

We have also tried using a model in which we assume first that the $(\bar{a}, \bar{b}, \bar{c})$ of a galaxy can only be taken from a finite set ($\sim$100 sets of $(\bar{a}, \bar{b}, \bar{c})$), and secondly that the relative abundance of galaxies with different $(\bar{a}, \bar{b}, \bar{c})$ are independent and to be determined via the linear decomposition of the real b/a–$\log a$ distribution. We finally discard this model because the large number of free parameters leads to severe overfitting, which made the results meaningless.

Given a multivariate Gaussian distribution of (E, T, γ), the probability that one observes a certain set of such parameters, $P\left((E, T, \gamma) \,|\, (\bar{E}, \bar{T}, \bar{\gamma}, \Sigma)\right)$ can be easily calculated. And for each set of (E, T, γ) we can calculate the probability distribution of its apparent $(b/a, \log a)$, i.e. $P((b/a, \log a)|(E, T, \gamma))$. Thus we can calculate the model b/a–$\log a$ distribution with the following formula:

$$
P\left(\left(\frac{b}{a}, \log a\right) \,|\, (\bar{E}, \bar{T}, \bar{\gamma}, \Sigma)\right) =
$$
$$
\sum P\left(\left(\frac{b}{a}, \log a\right) | (E, T, \gamma)\right) \cdot P\left((E, T, \gamma) | (\bar{E}, \bar{T}, \bar{\gamma}, \Sigma)\right) \quad (4)
$$

By similar renormalization and MCMC to the ones described in Section 3.2, we can find the best-fitting parameter set, which, in this case, is $(\bar{E}, \bar{T}, \bar{\gamma}, \Sigma)$.

4 RESULTS

4.1 Continuity of trends with redshift and mass

Before we show the quantitative results, we point out that there are some aspects evolving with time and mass that can be seen in Figs 2 and/or 4. As the redshift decreases and the mass increases, we see the following trends:

First, as is seen from Fig. 4, the b/a distribution gets more and more uniform, and the peak of the number density at small b/a gets less pronounced. For the late-discy bin, the distribution is rather flat over a large b/a range regardless of the size of a galaxy, which is characteristic of the growth of a discy population.

Secondly, in each panel of Fig. 2, the upper right corner where few objects populate at low mass and high redshift gets filled up at higher mass and lower redshift. From the visual inspections on the images of the galaxies that are appearing here we find that these objects are predominantly disc galaxies, with well-defined discs and bulges.

Also, the negative correlation between A_V and b/a in Fig. 2 gets more and more pronounced. This is also consistent with the growth of a discy population, because only the discy galaxies can have a larger path-length through the whole galaxy (and therefore a larger A_V value) and a smaller projected b/a value simultaneously.

Finally, we can see that there is a small tail of the b/a–$\log a$ distributions in most panels of Fig. 2 at the lower right corner, and it gets more pronounced with increasing time and mass. This is understandable under the hypothesis that the oblateness grows with time and mass, because when a discy galaxy is viewed in an edge-on configuration, it would possess a larger path-length at the centre, and a smaller one at the edge. Therefore the inner parts

of the image will be more attenuated by dust than the outskirts, making the light intensity decline slower with the radius. Given the definition of the half-light radius, a discy galaxy will therefore have a larger a when viewed edge-on than it has when viewed face-on. The growing significance of this feature with time and mass is yet more evidence for a growing discy population. The ellipsoidal model for edge-on discy galaxies used here exhibits *constant* semimajor axis as galaxies become more inclined and therefore does not model this extended tail to larger radii. However, an empirical method to correct for the tail had little impact on the modelling results (see Appendix), and thus we believe that the tail is not a serious problem for this work. See the full comparison between the modelling results with and without correction in the Appendix.

These trends are all consistent with the big picture that the oblateness (prolateness) of galaxies increases (decreases) with time and mass, which is the major conclusion of this work. It also serves as a sanity check on our quantitative modelling results, in the sense that a reasonable modelling should give an increasing fraction of discy objects with time and mass.

4.2 Empirical modelling results

We turn now to the results of more complex models, starting with the empirical model described in Section 3.2, which fits all b/a–$\log a$ distributions as combinations of low-mass high-z galaxies (early-prolate bin) and high-mass low-z galaxies (late-discy bin). Fig. 6 shows the results of this fit for one mass-redshift panel (0.5 $< z <$ 1.0 and 9.5 $< \log (M_*/M_\odot) <$ 10), including the observed data, the best-fitting model, and the residual map. Fig. 7 shows the evolving trends of the relative weight f of the early-prolate bin in the decomposition with time and mass given by this empirical modelling. As we can see, the importance of the elongated galaxies decreases with increasing time and mass. Fig. 8 summarizes the fractions of the three shapes of galaxies in all the redshift and mass bins given by the empirical modelling. To obtain these values, we assume the fractions in a certain redshift and mass bin are linear combinations of those in the early-prolate bin and the late-discy bin, weighted by the same weights as the b/a–$\log a$ distribution itself, while the fractions of the two extreme bins are obtained from ETa modelling. From Figs 7 and 8 it appears that the oblateness (prolateness) increases (decreases) with increasing time and mass, which is consistent with the continuous evolution discussed in Section 4.1.

Nevertheless, we do see some systematic patterns in the residual maps of such empirical fittings (e.g. the residual map of Fig. 6), which is not surprising, because even though the b/a–$\log a$ distributions evolve smoothly, it is unreasonable to expect that all such mass-redshift bins can be fit perfectly with two extrema.

4.3 ETa modelling results

Here we present the results of the ETa modelling for all the redshift-mass bins. To be concise, Figs 9 and 10 show relevant plots (i.e. the observed distribution, the model distribution, the residual map, and the model distributions of galaxies of the three shapes defined by Fig. 1) only for the two extrema among all the bins, namely the late-discy bin and the early-prolate bin.[3] In all panels but panel (c) of Figs 9 and 10, each bin is colour coded by the number of galaxies

---

[3]Similar plots illustrating the rest of redshift-mass bins can be found at https://sites.google.com/site/zhw11387/Home/research
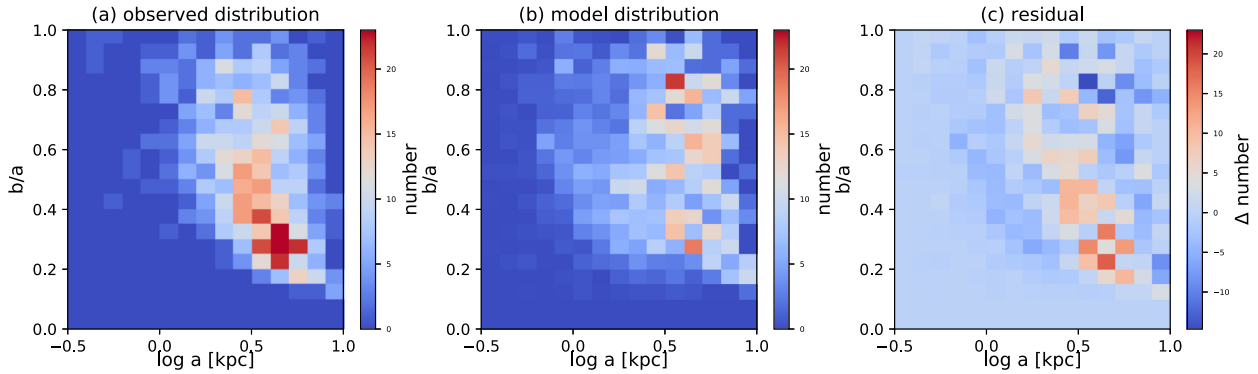
Figure 6. The empirical modelling results of the galaxies with $0.5 < z < 1.0$ and $9.5 < \log(M_*/M_\odot) < 10$. Panel (a): The observed b/a–$\log a$ distribution. Panel (b): The model distribution. Panel (c): The residual map. All bins are colour coded by the (Δ) numbers of the galaxies in them. The model distribution is a linear combination of those of the early-prolate bin and the late-discy bin, and renormalized so that the model has the same number of galaxies as the real observed data. A non-negligible systematic pattern is clearly seen in the residual map, which indicates that the empirical model is not a perfect fit.
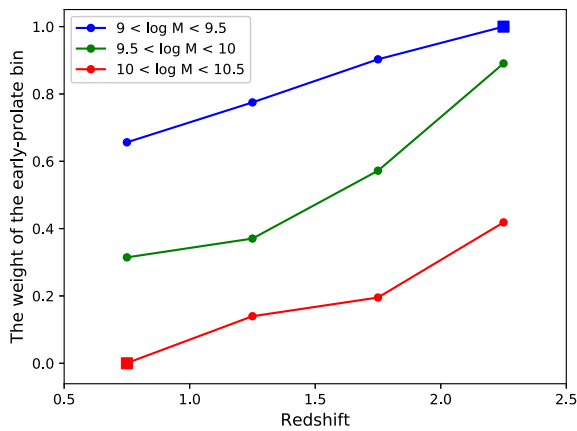
[htb]

Figure 7. The evolving trend of the relative weight of the early-prolate bin with time and mass. The squares denote the cases in which the early-prolate or late-discy bins are themselves modelled, so the weight of the early-prolate bin is naturally unity or zero.

therein, while panel (c) shows the distribution of the galaxy number differences between the first two panels. Panel (d)–(f) shows the number distributions contributed by three different kinds of galaxy shapes, which are defined using intrinsic $\bar{c}/\bar{a}$ and $\bar{b}/\bar{a}$ in Fig. 1. These three panels basically describes which part of the projected b/a–$\log a$ space the elongated, discy, and spheroidal galaxies take up, and what their number distributions are in each b/a–$\log a$ bin, given that the number of galaxies in the model is the same as in the observed data.

From Figs 9 and 10 we can immediately see that the early-prolate and late-discy bins are indeed dominated by elongated and discy galaxies, respectively. All the b/a–$\log a$ bins are colour coded by the number of (either real or model) galaxies in them. In the early-prolate bin, most of the galaxies are elongated, especially in the lower right corner of the projected b/a–$\log a$ diagram, while in the late-discy bin, we can barely find any elongated objects. The best-fitting parameters and the fractions of the three galaxy shapes of each redshift-mass bin are tabulated in Table 1. For the most massive bins, there are too few galaxies for the bootstrap algorithm to get a realistic estimation of the uncertainties of the parameters; thus we only present the best-fitting parameters values without errors. Qualitatively the fraction of elongated (discy)

galaxies in the early-prolate (late-discy) bin is consistent with what van der Wel et al. (2014) found. But our results differ from the previous work in the sense that we find more elongated and/or spheroidal galaxies and fewer discy objects than van der Wel et al. (2014), especially in the low-redshift and low-mass bins. This is expected because modelling the marginalized projected b/a distribution is likely to mistake large elongated galaxies and small round galaxies for discy objects, given the fact that the smaller galaxies tend to be rounder. To illustrate this point we further present Fig. 11, the panel (a) of which shows the b/a distributions of the larger, smaller, and all the galaxies with $0.5 < z < 1.0$ and $9.5 < \log(M_*/M_\odot) < 10$, and panel (b) shows the b/a distribution of all the galaxies analysed by van der Wel et al. (2014) in that redshift-mass bin. It is clear seen from Fig. 11(a) that the smaller galaxies have a broad and somewhat flat distribution of b/a at $b/a \gtrsim 0.4$ (blue open histogram), which is indicative of a spheroidal population (maybe marginally discy) according to the definitions shown in Fig. 1. On the other hand, the b/a distribution of the larger galaxies (red open histogram) shows a significant peak at $b/a \sim 0.25$, and declines as b/a increases. This is strongly characteristic of an elongated population with an intrinsic $\bar{c}/\bar{a} \sim 0.25$. However, by marginalizing over the $\log a$ dimension (i.e. superposing the red and the blue histogram), we get a relatively broad and flat b/a distribution over a large b/a distribution, which is very similar to the distribution shown in Fig. 11(b) that was analysed by van der Wel et al. (2014). Therefore we argue that van der Wel et al. (2014) end up misidentifying small objects with median b/a and large ones with $b/a \sim 0.25$ as discy galaxies. From this example we can see that adding the dimension of galaxy size helps to avoid such misidentifications, which is one of the main points of this work. Our modelling results in Figs 9 and 10 also match our intuition that spheroidal galaxies are predominantly smaller than elongated and discy galaxies.

Fig. 12 shows the evolution with redshift and mass of the $\bar{b}/\bar{a}$–$\bar{c}/\bar{a}$ distributions generated by the best-fitting parameters listed in Table 1. The yellow lines are the boundaries between different galaxy shapes as defined in Fig. 1. From this figure we can see that the majority of elongated galaxies, if any, are actually prolate objects with $\bar{b} \sim \bar{c} < \bar{a}$, which is why we call the least massive and highest redshift bin as the 'early-prolate' bin. Another feature we can see is that the peak of the $\bar{b}/\bar{a}$ distributions generally moves from the elongated region to the discy/spheroidal region, which is another confirmation of the picture that the oblateness (prolateness)
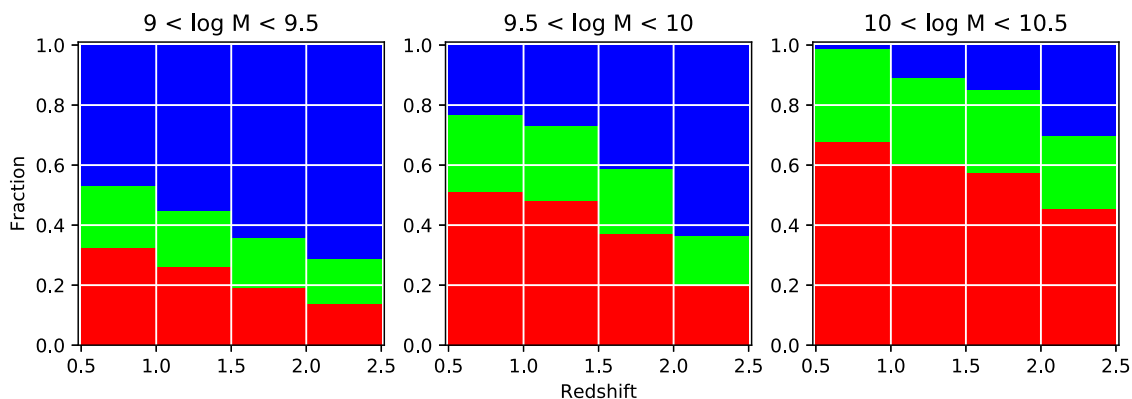
Figure 8. The evolution of the fractions of different shapes of the star-forming galaxies in CANDELS with redshift and stellar mass, given by the empirical modelling. Blue bars: The fractions of elongated galaxies. Green bars: The fractions of spheroidal galaxies. Red bars: The fractions of discy galaxies. Compare with the ETa modelling results in Fig. 13.
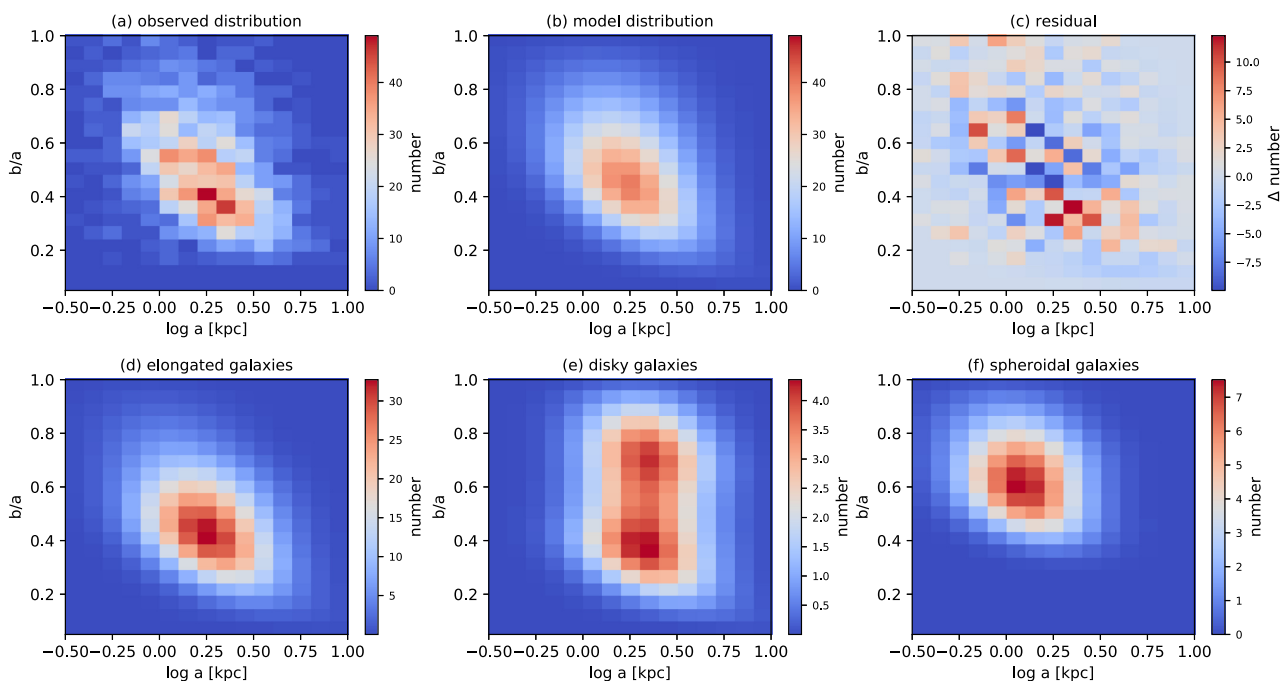

Figure 9. Illustrative plots of the fitting results for the b/a–$\log a$ distribution of galaxies in the early-prolate bin. Panel (a): observed data distribution. Panel (b): best-fitting model distribution. Panel (c): residual map. Panel (d)–(f) describes given the best-fitting model, which part of the projected b/a–$\log a$ space the elongated, discy, and spheroidal galaxies would take up, and what their number distributions are in each b/a–$\log a$ bin, given that the number of galaxies in the model is the same as in the observed data. Note that the ranges of colour bars are different for Panel (d)–(f) and the smaller numbers of discy and spheroid galaxies compared with elongated ones.

increases (decreases) with increasing time and mass. An exception is the galaxies with $1.0 < z < 1.5$ and $10.0 < \log (M_*/M_\odot) < 10.5$, whose b/a distribution is significantly tighter than the rest of the bins. This is ultimately due to the fact that the best-fitting value of the Gaussian variance in the traxiality T for this bin is only 0.007 (see Table 1). Given the definition of T (i.e. $T = (\bar{a}^2 - \bar{b}^2)/(\bar{a}^2 - \bar{c}^2)$), a small Gaussian spread in T means that the intrinsic $\bar{b}/\bar{a}$ is essentially a function of $\bar{c}/\bar{a}$. Given the best-fitting mean value of $T = 0.36$, $\bar{b}/\bar{a}$ as a function of $\bar{c}/\bar{a}$ tells us that galaxies nearly cannot have an elongated shape as defined by Fig. 1. That said, we are currently not sure about the reason why the fitting gives such tight distribution of T. We note that this happens in one of the most massive bins with relatively smaller number of galaxies compared to less massive

ones. So the small sample size may be the cause, since we use Poisson statistics in the calculation of the likelihood in MCMC. We expect larger surveys covering more galaxies in this redshift-mass bin to resolve this issue.

Fig. 13 shows the evolution trends of the three fractions with time and stellar mass. Again we can see a general trend that the fraction of elongated (discy) galaxies decreases (increases) with time and mass, consistent with the picture that discy galaxies emerge and come to dominate the whole galaxy population with the cosmic time and the stellar mass of galaxies, which is in good agreement with the trend seen in Fig. 8. By comparing this plot with fig. 4 of van der Wel et al. (2014), we further confirm that we find more elongated and/or spheroidal galaxies than they did.
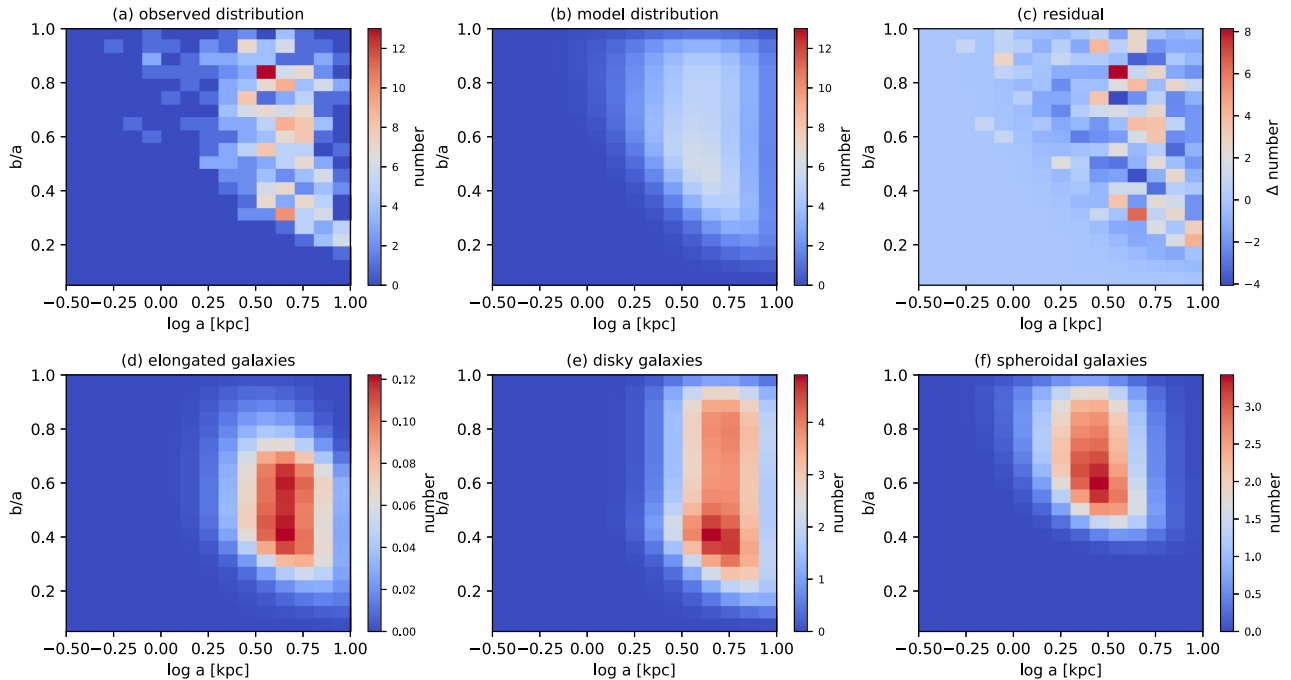
Figure 10. The same plots as Fig. 9, but for the galaxies in the late-discy bin. Note that the bin has the smallest number of galaxies at any bin.

4.4 Massive galaxies with $10.5 < \log(M_*/M_\odot) < 11.0$

As can be seen from Fig. 2, the numbers of galaxies in the most massive bins are too small to be modelled robustly. But some qualitative comments can still be made.

First we can clearly see that the curved boundary gets less and less pronounced as time goes by. There are two compatible explanations to this phenomenon: It can be either due to the fact that the number of elongated galaxies decreases with time and the discy objects get more and more prevalent, so that the curved boundary, which is a natural outcome of a dominant elongated population, gradually fades out and a flat distribution over a large projected *b/a* range takes its place. Alternatively, it can be due to the disappearance of the small and round star-forming galaxies. They start to quench and consequently drop out of the star-forming sample with time, leaving the upper left corner of the *b/a*–log *a* diagram less and less populated. See Barro et al. (2013) for more details of such a process.

The second trend to be seen in Fig. 2 is that the correlation between A_V values and *b/a* improves with time and mass. At high redshift, there is barely a systematic trend of A_V value with *b/a*, while as we move to lower redshift bins, the correlation gets more and more significant. At the late-discy bin, the negative correlation between A_V and *b/a* is the most pronounced. This evolution of the negative correlation is consistent with the picture that the oblateness grows with time and mass and that the high-A_V objects are discy edge-on galaxies with large dust path-lengths at late cosmic times.

5 DISCUSSION

5.1 The probabilities of a galaxy being elongated, discy, or spheroidal

Given the best-fitting model, we can easily calculate the numbers of elongated, discy, or spheroidal galaxies in an arbitrary *b/a*–log *a* bin of CANDELS. If we further divide these numbers by the total numbers of galaxies in this bin we can get the probabilities of

having a certain class of shape at a given set of projected (*b/a*, log *a*). Since the *b/a*–log *a* distribution evolves with time and mass, this modelling effectively enables us to predict how likely a galaxy is to be intrinsically elongated, discy, or spheroidal *as a function of its redshift, stellar mass, projected b/a*, and log *a*. Figs 14 and 15 show such probability distributions for the star-forming galaxies in the high-z low-mass (early-prolate) and low-z high-mass (late-discy) bins, respectively.[4] As can be seen in both plots, the probability of being discy at large log *a* and *b/a* is always high (typically with a value of 0.7–1.0), while the probability of being elongated at the lower right corner depends on time and mass. For the early-prolate bin, due to the dominance of the elongated population, the probability is high at this corner, since elongated galaxies are much more likely to show up at this region; while in the late-discy bin, our modelling finds barely any elongated galaxies, which results in a high probability of being discy for a galaxy in this lower right region. As for the probabilities of being spheroidal, in both bins they peak at the upper left corner, which is consistent with our intuition that galaxies are intrinsically rounder when we look at smaller objects. Such probability maps can facilitate future morphological and kinematic observations aimed at searching for elongated galaxies at a range of redshifts, including at $z > 3$ with *James Webb Space Telescope* (*JWST*).

5.2 Comparison with VELA simulation images

We have pointed out that our results show growing oblateness of star-forming galaxies with time and stellar mass, which is also seen in the VELA simulations. However, Ceverino et al. (2015) and Tomassetti et al. (2016) investigated the evolution of the three-dimensional *mass* profile in the VELA galaxies, while what we have modelled are the distributions of *b/a* and log *a* measured from

---

[4]Such probability maps illustrating the rest of the redshift and mass bins can be found at https://sites.google.com/site/zhw11387/Home/research.

Table 1. Best-fitting model parameters and fractions of the three shapes of each redshift-mass bin.

Redshift	$\log(M_*/M_\odot)$	$\bar{E}^a$	$\bar{T}^b$	$\bar{\gamma} = \langle \log a \rangle^c$	$\mathrm{Var}(E)^d$	$\mathrm{Var}(T)$	$\mathrm{Var}(\gamma)$	$\mathrm{Cov}\langle E, \gamma \rangle$	$f_{\mathrm{elongated}}$	f_{discy}^e	$f_{\mathrm{spheroidal}}^e$	N_{galaxy}
0.75	9.25	0.747 ± 0.005	0.49 ± 0.07	0.462 ± 0.005	0.009 ± 0.002	0.77 ± 0.04	0.046 ± 0.002	0.018 ± 0.002	0.376 ± 0.008	0.51 ± 0.01	0.12 ± 0.01	2071
0.75	9.75	0.74 ± 0.01	0.16 ± 0.08	0.57 ± 0.01	0.008 ± 0.006	0.66 ± 0.07	0.043 ± 0.003	0.016 ± 0.005	0.324 ± 0.009	0.56 ± 0.03	0.12 ± 0.03	1024
0.75	10.25	0.728	0.166	0.680	0.035	0.039	0.062	0.038	0.013	0.678	0.309	426
1.25	9.25	0.740 ± 0.003	0.85 ± 0.01	0.436 ± 0.003	0.009 ± 0.002	0.21 ± 0.02	0.047 ± 0.002	0.017 ± 0.001	0.53 ± 0.01	0.33 ± 0.02	0.13 ± 0.01	2531
1.25	9.75	0.711 ± 0.004	0.2 ± 0.1	0.527 ± 0.007	0.012 ± 0.005	0.4 ± 0.1	0.048 ± 0.002	0.020 ± 0.003	0.28 ± 0.02	0.49 ± 0.04	0.23 ± 0.02	1319
1.25	10.25	0.659	0.362	0.604	0.016	0.007	0.050	0.023	0.003	0.541	0.456	525
1.75	9.25	0.736 ± 0.004	0.978 ± 0.004	0.397 ± 0.004	0.009 ± 0.002	0.13 ± 0.01	0.048 ± 0.002	0.014 ± 0.002	0.68 ± 0.01	0.20 ± 0.02	0.118 ± 0.009	2714
1.75	9.75	0.710 ± 0.004	0.93 ± 0.01	0.496 ± 0.005	0.013 ± 0.003	0.32 ± 0.03	0.050 ± 0.003	0.020 ± 0.002	0.31 ± 0.01	0.46 ± 0.02	0.23 ± 0.01	1349
1.75	10.25	0.673	0.570	0.619	0.020	0.577	0.057	0.027	0.295	0.338	0.367	464
2.25	9.25	0.74 ± 0.03	0.98 ± 0.02	0.313 ± 0.008	0.01 ± 0.01	0.10 ± 0.05	0.052 ± 0.003	0.014 ± 0.004	0.71 ± 0.06	0.14 ± 0.09	0.15 ± 0.03	2099
2.25	9.75	0.71 ± 0.02	0.96 ± 0.01	0.40 ± 0.01	0.008 ± 0.006	0.15 ± 0.04	0.041 ± 0.002	0.011 ± 0.002	0.62 ± 0.05	0.20 ± 0.06	0.18 ± 0.02	1239
2.25	10.25	0.642	0.802	0.492	0.014	0.295	0.050	0.018	0.348	0.229	0.423	550

$^a E = 1 - \bar{c}/\bar{a}$ is the ellipticity of a galaxy.

$^b T = (\bar{a}^2 - \bar{b}^2)/(\bar{a}^2 - \bar{c}^2)$ is the triaxiality of a galaxy.

$^c \gamma = \log a$.

$^d \mathrm{Var}(E)$ is the variance of the Gaussian distribution of E.

^{e}The definitions of the three shapes are from the boundaries in Fig. 4.

For the $10 < \log(M_*/M_\odot) < 10.5$ bins, the bootstrap algorithm give unrealistic uncertainties due to the relative smaller numbers of observed galaxies in these bins, thus we only present the best-fitting parameter values without errors.
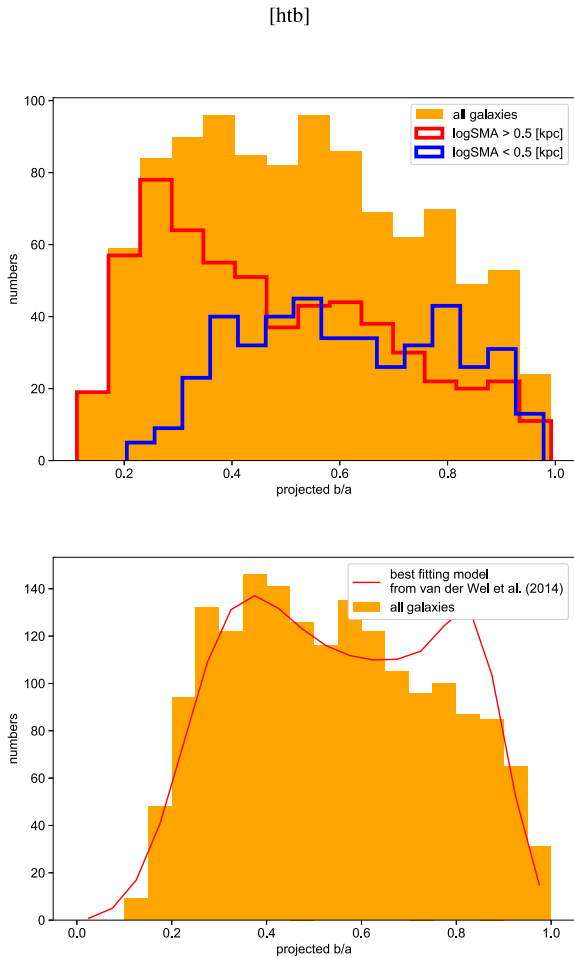
[htb]

Figure 11. Panel (a): The *b/a* distribution of the CANDELS galaxies with $0.5 < z < 1.0$ and $9.5 < \log(M_*/\mathrm{M_\odot}) < 10$. Red open histogram: *b/a* distribution of larger galaxies with $\log a > 0.5$. Blue open histogram: the same distribution of smaller galaxies with $\log a < 0.5$. Orange filled histogram: the same distribution of all the galaxies in that redshift-mass bin. Panel (b): The *b/a* distribution of the 3D-*HST* galaxies with $0.5 < z < 1.0$ and $9.5 < \log(M_*/\mathrm{M_\odot}) < 10$ (the one that was analysed by van der Wel et al. (2014)). Orange filled histogram: *b/a* distribution of all the galaxies in that redshift-mass bin. Red Curve: the best-fitting model obtained by van der Wel et al. (2014).

the *light* profiles of the galaxies. Thus a more direct comparison between the light profiles of CANDELS and VELA galaxies is necessary.

To support the argument that our claimed detection of prolate galaxies in most mass and redshift bins is real (mostly at the lower right corner of the *b/a* − log *a* diagram), we have inspected numerous multiwaveband images of CANDELS galaxies in that corner and those of VELA prolate galaxies. Fig. 16 shows two such images. Fig. 16(a) is a typical galaxy located at the lower right corner of the *b/a*–log *a* diagram from CANDELS, and Fig. 16(b) is a galaxy in its prolate phase at redshift $z = 1.32$ in the VELA05 simulation. We can see that the two galaxy images share some common features: a brighter centroid with symmetric and extended linear structure. Given the similarity between the morphologies of these two galaxies, it is quite plausible that many galaxies in the lower right corner are indeed prolate, and pure visual inspection of the images is not sufficient to tell prolate or other elongated objects

from discs because they can be very similar in their projected light profiles.

Besides totally qualitative comparisons based on the visual inspections on the images, we also compare the *b/a*–log *a* distributions of the galaxies from CANDELS and those whose mass profile shapes are in the elongated region of Fig. 1 from the VELA simulation. Fig. 17(a) shows the distribution of CANDELS galaxies in the early-prolate bin, and Fig. 17(b) shows that of the elongated galaxies in the VELA simulation. In this panel we define as elongated objects with a three-dimensional mass profile shape obtained by Tomassetti et al. (2016) that places them in the elongated region as defined by Fig. 1. We included all the elongated galaxies with $1 < z < 3$ viewed from truly random camera directions in Fig. 17(b), regardless of their masses, because the VELA simulations include rather few simulated galaxies (only 34 galaxies in the simulations, six of which are included in Fig. 17b). The statistics about the log *a* and *b/a* of these two samples are included in Table 2.

From both the visual inspection on Fig. 17 and the statistics shown in Table 2 we can see that the *b/a*–log *a* distributions of these two samples are consistent with each other, if we take into account the small number of points in the VELA sample. Specifically, they share the following features:

(1) clear curved lower boundaries from the small and round region $(-0.2 < \log a < 0, b/a > 0.6)$ to the large and elongated region $(0.6 < \log a < 1.0, 0.2 < b/a < 0.4)$;

(2) low frequency of objects at the upper right corner.

All of these are consistent with a population dominated by elongated galaxies. Therefore this serves as further supporting evidence that our modelling results are plausible. We also note that the VELA galaxies seems slightly rounder than the CANDELS galaxies, which can be seen from both the comparison between the two panels of Fig. 17. We suggest that this is the result of the small number statistics of the VELA galaxies, given the fact that there are merely 34 galaxies observed from different directions at a series of time-steps, and that this small quantitative difference does not change our main qualitative conclusions.

A third comparison between the CANDELS data and the VELA simulation data can be done in terms of the time evolution of the fractions of different shapes of galaxy stellar mass distributions. Before going into the comparison, we point out that many VELA galaxies do not reach a phase where they have a very small intrinsic *c/a*, and also that in the $\bar{c}/\bar{a}$–$\bar{b}/\bar{a}$ parameter space there is a cluster of galaxies right at the boundary between the discy and spheroidal galaxies as defined by Fig. 1. We therefore argue that in order to do a fair comparison, figuring out new definitions of the shape of the galaxies is necessary. Fig. 18 shows the distribution of the mass profiles of the VELA galaxies in $\bar{c}/\bar{a}$–$\bar{b}/\bar{a}$ parameter space, along with new boundaries between different shapes. Each point corresponds to a galaxy at a time-step, colour coded by its redshift.

To study the effect of stellar mass on the shape evolution we need to find criteria differentiating between larger and smaller VELA galaxies. We split the whole VELA sample into more massive galaxies and less massive ones using a critical stellar mass at a certain time-step (in the VELA simulations, each time-step is labelled with the scale factor of the universe $a_{\exp}$). By visual inspection on the M_*–$a_{\exp}$ diagram, we choose $M_* = 6 \times 10^9\,\mathrm{M_\odot}$ at $a_{\exp} = 0.26$ ($z = 2.85$) as the critical mass. Galaxies with M_* below (above) this value at $a_{\exp} = 0.26$ are called low-mass (high-mass) galaxies.
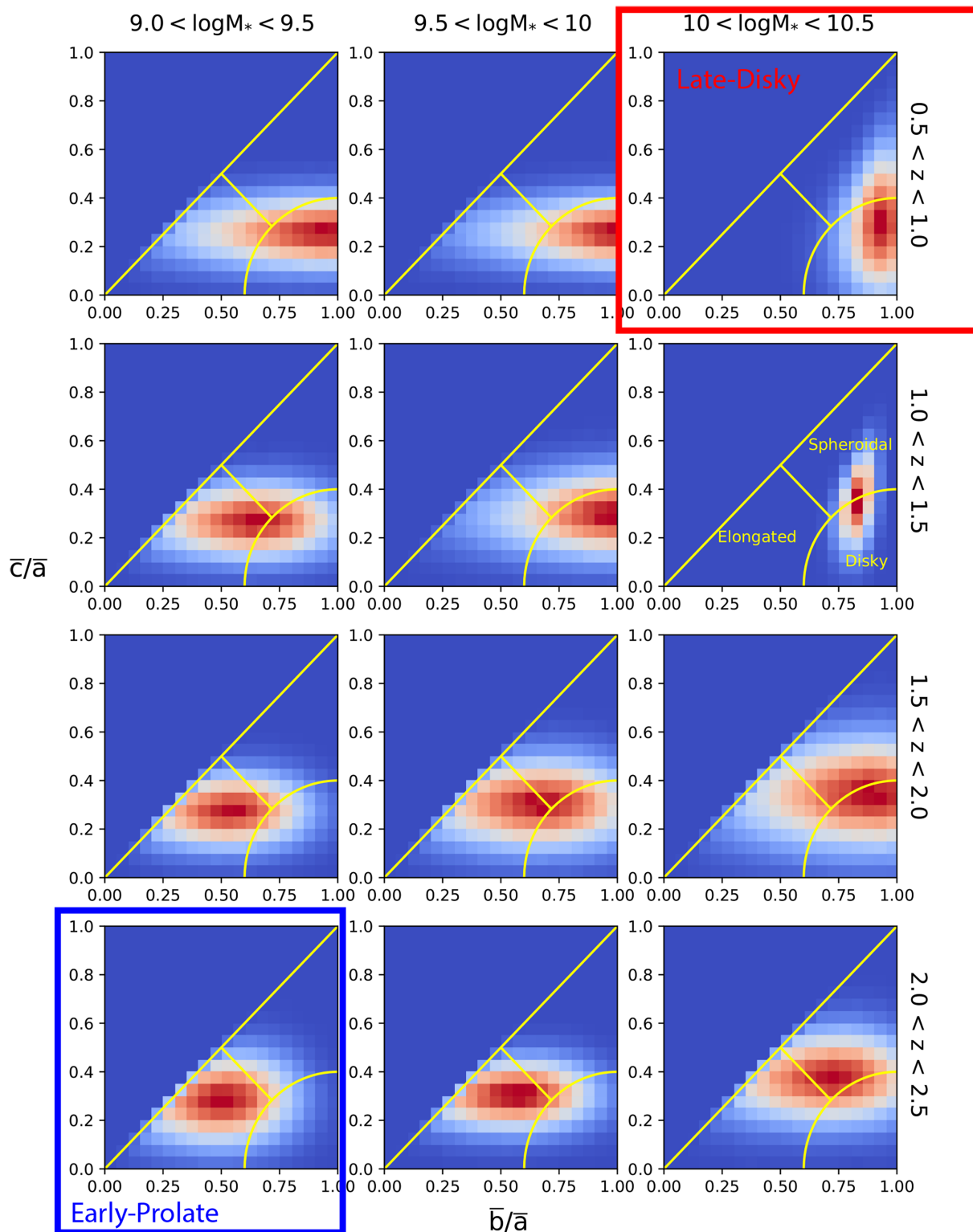
Figure 12. The evolution of the $\bar{b}/\bar{a}$–$\bar{c}/\bar{a}$ distributions with redshift and mass. The distributions are generated by the best-fitting parameters listed in Table 1. The yellow lines are the boundaries between different galaxy shapes as defined in Fig. 1. The redder colour means larger densities of the distribution. Note the evolving trend with increasing time and mass that the peak of the distributions gradually move from the elongated region to the discy/spheroidal region. The early-prolate bin and late-discy bin, as defined in the caption of Fig. 2 and Section 3.2, are squared in blue and red, respectively.

Based on these definitions, we can now investigate the time evolution of the fractions of different shapes of the galaxies in different mass bins. Fig. 19 shows two such evolutions for low-

and high-mass galaxies. From both panels a clear trend is seen that the fractions of the elongated (settled) galaxies decrease (increase) with time. Furthermore we can see that at a given redshift, the
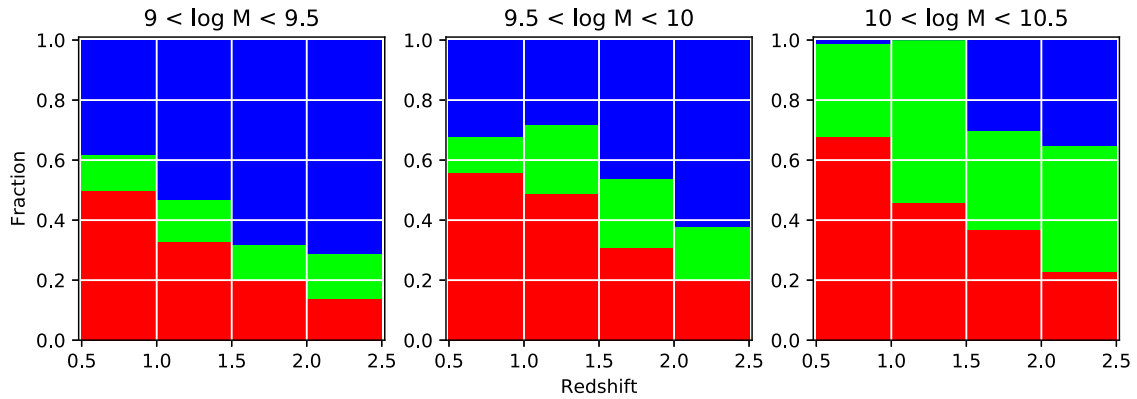
Figure 13. The evolution of the fractions of different shapes of the star-forming galaxies in CANDELS with redshift and stellar mass, given by the ETa modelling. Blue bars: The fractions of elongated galaxies. Green bars: The fractions of spheroidal galaxies. Red bars: The fractions of discy galaxies. These fractions are qualitatively in good agreement with those obtained by the empirical modelling in Fig. 8.
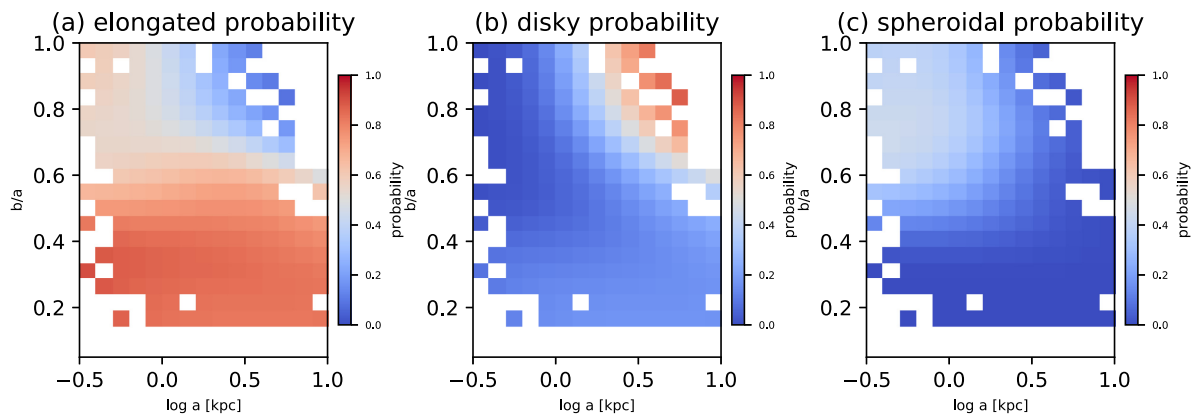

Figure 14. The probability distribution of a CANDELS galaxy's being elongated, discy, or spheroidal over the b/a–$\log a$ plane for the early-prolate bin. Probabilities are only calculated in the bins containing at least one observed galaxy.
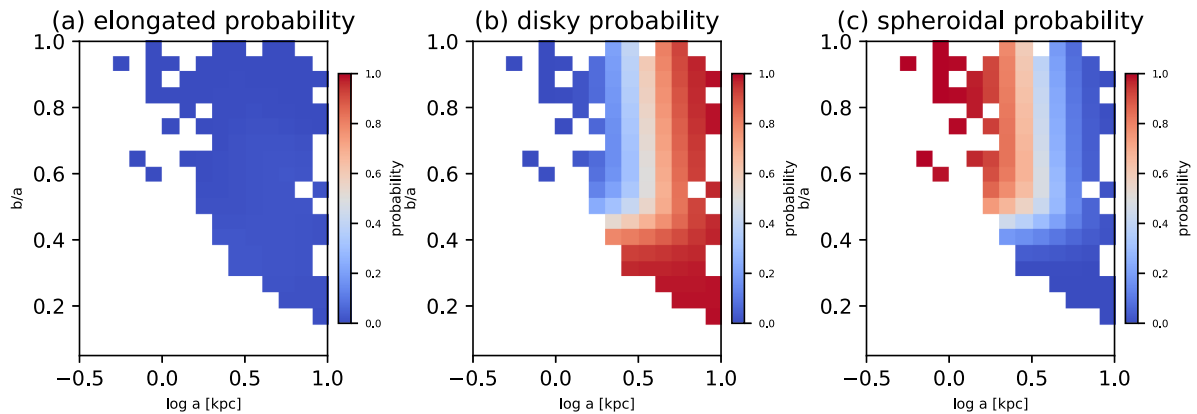
Figure 15. The probability distribution of a CANDELS galaxy's being elongated, discy, or spheroidal over the b/a–$\log a$ plane, for redshift and mass interval for the late-discy bin. Probabilities are only calculated in the bins containing at least one observed galaxy.

fraction of the elongated objects among the more massive galaxies is smaller than it is among the less massive ones. In other words, the less massive galaxies are evolving like the more massive ones, but their evolution is relatively delayed in time. These trends, again, are consistent with the modelling of CANDELS b/a–$\log a$ distributions above (both the ETa and the empirical models), with the finding by Jiang et al. (2018) that the intermediate isophotes of more massive galaxies at lower redshift are more discy, with previous analysis on

the evolution of three-dimensional shapes of the VELA galaxies by Ceverino et al. (2015, see fig. 2) and Tomassetti et al. (2016, see fig. 7), with kinematic observations of real galaxies by Kassin et al. (2012) and Simons et al. (2016, 2017), and with kinematic calculations of simulated galaxies by Kassin et al. (2014) and Ceverino et al. (2017) that found an increasing rotational support with time in star-forming galaxies.
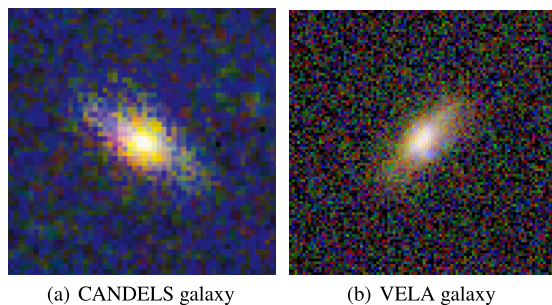
(a) CANDELS galaxy   (b) VELA galaxy

Figure 16. Panel (a): an example of a large and elongated galaxy in CANDELS. This galaxy has a $z = 2.27$ and $\log(M_*/M_\odot) = 9.82$. Panel (b): image of the simulated galaxy VELA05 at $z = 1.32$, which has a prolate three-dimensional mass profile shape, including the effects of stellar evolution, dust scattering and absorption, the *HST*/WFC3 PSF, and sky background. Despite the bulge+disc appearance of the VELA galaxy, it is in fact prolate, showing that true 3D shapes cannot be reliably measured from projected images alone. The CANDELS galaxy, with similar appearance, is a member of a mass-redshift bin where most galaxies are modelled as prolate.

Finally, we note that in the VELA simulations there is a gradual transition from prolate to discy that tends to occur when the galaxy is in the vicinity of a characteristic stellar mass, $10^{9.5–10.0}\,M_\odot$, and this transition mass does not show a significant variation with redshift (Tomassetti et al. 2016). Typical masses in the same range are associated with the major wet compaction into a blue nugget (BN) phase that triggers central quenching, and causes transitions in most structural, kinematic, and compositional galaxy properties (Zolotov et al. 2015; Tacchella et al. 2016a; Tacchella et al. 2016b). In the CANDELS data we find some hints for a similar mass dependence of the shape, transitioning from prolate to discy in roughly the same mass range, but with the transition mass varying with redshift, since we can see from Fig. 8 that the stellar mass ranges at which the fractions of elongated galaxies drops below 50 per cent increases with increasing redshift. A similar finding is made by Huertas-Company et al. (2018) that the transition into the BN phase of galaxies happens preferentially in a stellar mass range of $10^{9.2–10.3}\,M_\odot$ at all redshifts, and that the characteristic mass increases as one looks at higher redshifts. This may be a real difference between the simulations and observations, and if so it is worth putting forward as an interesting challenge for theoretical understanding. However, in principle it could also be due to systematics in the shape analysis and/or in the selection, either in the simulations or in the observations. For example, a transition-mass range that is decreasing with time may appear in the simulated sample as constant with time because the masses are monotonically increasing with time. Further discussions on the characteristic mass when the shape transitions happen is beyond the scope of this work, and we refer the readers to Huertas-Company et al. (2018) for more insights on this topic, especially their figs 13 and 16, where the fractions of galaxies in the pre-BN, BN, and post-BN phases are shown as a function of stellar mass at different redshift ranges.

6 CAVEATS

In this section, we summarize a number of potential problems with the analysis in this paper.
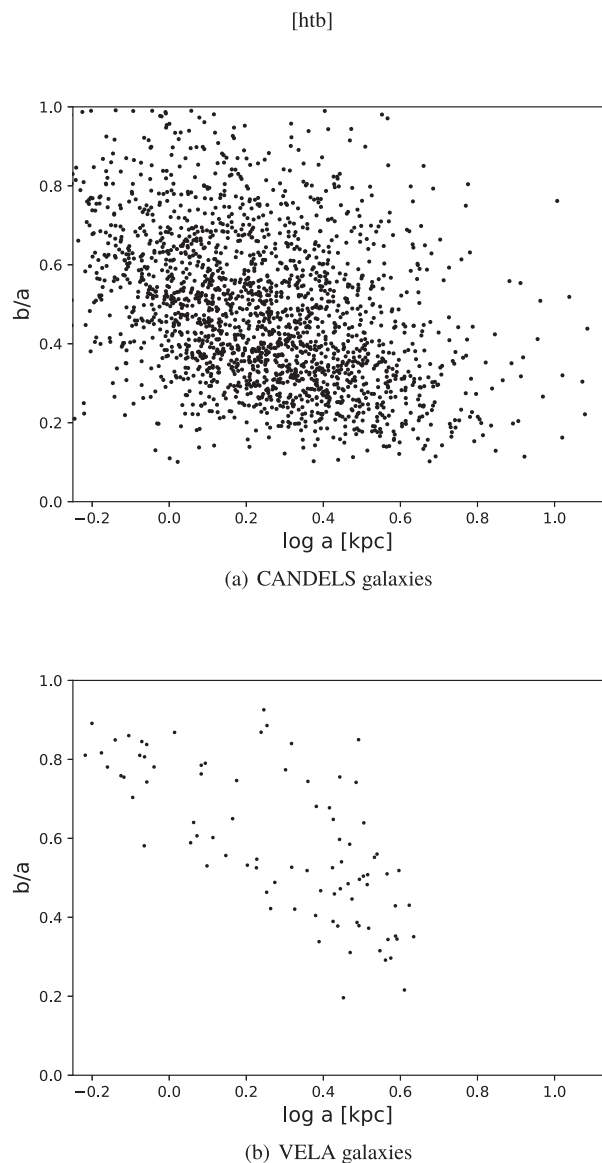
[htb]

(a) CANDELS galaxies

(b) VELA galaxies

Figure 17. Panel (a): the b/a–$\log a$ distribution of CANDELS star-forming galaxies in the early-prolate bin. Panel (b): The same distribution of elongated VELA galaxies in all mass-redshift bins. Elongated galaxies are defined as having a three-dimensional mass profile shape obtained by Tomassetti et al. (2016) that places them in the elongated region defined by Fig. 1. Only the truly random images as defined in Section 2.3 are plotted. There is an overall agreement between the model and observed distributions, but the VELA galaxies are on systematically rounder and larger in size than the CANDELS galaxies.

Table 2. Statistics about the $\log a$ and b/a of the galaxies in the two samples in Fig. 17.

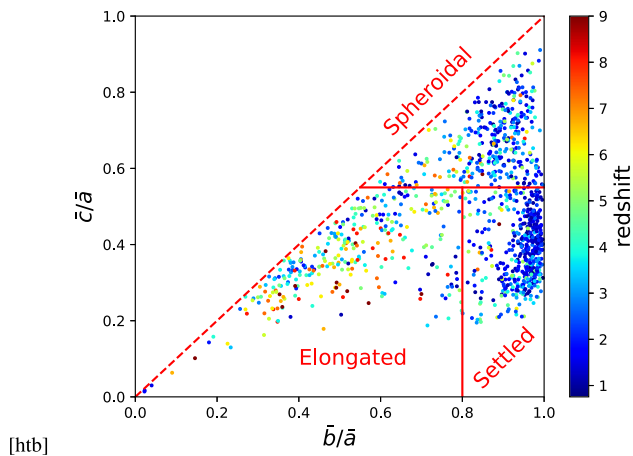| Sample	$\langle \log a \rangle$	$\sigma_{\log a}$	$\langle b/a \rangle$	$\sigma_{b/a}$
CANDELS	0.24	0.26	0.48	0.19
VELA	0.29	0.25	0.59	0.18

Figure 18. The $\bar{c}/\bar{a}$–$\bar{b}/\bar{a}$ distribution of the VELA galaxies throughout the simulation. Each dot denotes the mass profile of a galaxy at a certain time-step, which was obtained by Tomassetti et al. (2016), colour coded by its redshift. The red solid lines are the boundaries between different shapes of galaxies. The red dashed line is the physical boundary where $\bar{c} = \bar{b}$.

Our modelling is based on the fundamental assumption that a galaxy can be modelled as a uniform three-dimensional ellipsoid, and when viewed from a certain direction, the observed b/a and a are calculated from the projection of that ellipsoid. A more realistic modelling is to model the galaxies as single Sérsic light profiles and get their apparent b/a–$\log a$ distribution by generating randomly viewed mock images with the method introduced by van de Ven & van der Wel (in preparation), and measuring these images with GALFIT. See the Appendix for a discussion in more detail about such a Sérsic modelling. Due to the limitation set by the available computational resources we are currently unable to calculate full b/a–$\log a$ distributions for these more realistic models. But based on the similarity between the distributions shown in Fig. 5, we argue that our main conclusions will not change qualitatively if we implement this more realistic Sérsic modelling.

Also, as can be seen from Figs 10 and 11, a few galaxies have a measured $\log \mathrm{SMA} \sim -0.5$, which roughly corresponds to 1/5 the size of the diffraction limit of *HST*. We chose to keep them in our sample because they are acceptable GALFIT results according to van der Wel et al. (2012), and better observations for these small objects are needed to tell whether these measurements are biased and whether our results are influenced. Another issue related to the measurement of galaxy properties is that the rest-frame 4600 Å luminosity of a galaxy given a stellar mass can vary by a large factor, which is determined by when the stellar mass was formed. This may lead to some bias when we try connecting the light profile to that of the stellar mass of a galaxy.

On the other hand, we have assumed that the galaxy population in each redshift and mass bin has a multivariate normal distribution in $(E, T, \gamma = \log a)$ parameter space. This assumption is a potential source of systematic effect that the modelled intrinsic $\bar{b}/\bar{a}$–$\bar{c}/\bar{a}$ distributions do not look like that of the *mass profiles* of the VELA galaxies, in the sense that the latter has many objects in highly spheroidal regions, and few galaxies in the intermediate region between elongated and settled galaxies as defined by Fig. 18, while the opposite is the case for the modelled distributions based on CANDELS data. In principle, it may also be the source of the redshift dependence of the transition mass range, at which a galaxy leaves the elongated phase and settles into disc galaxies, if the

transition mass range is in fact independent of time, as is the case in VELA simulations.

A third point is that our analysis method requires binning the data in two dimensions, which means that the numbers of objects in each bin are inevitably smaller than they are in one-dimensional b/a modellings. In this work, a typical b/a–$\log a$ bin contains a few dozen objects, while in van der Wel et al. (2014) it is common to see more than 100 galaxies in a single b/a bin. This makes the results less statistically robust than the ones from previous work. Hopefully in the future it will be possible to get a larger sample of star-forming galaxies to address this problem. But given the fact that the modelled distribution captures the features of the observed data well, and that parameters vary smoothly and regularly between adjacent mass-redshift bins, we argue that our results are also quite robust.

Another caveat concerns the completeness of the galaxies in the highest redshift bins. According to our selection criterion based on total magnitudes, the samples are nominally complete in every mass-redshift bin. However, in practice the catalogues may be incomplete near the magnitude limit due to loss of low-surface brightness galaxies. We believe this fact explains why, in Table 1, for the two less massive bins, the number of galaxies in the highest redshift bin is smaller than that in the next highest redshift bin. But we argue that this fact does not qualitatively change the main conclusions of this work. First, even if we remove all the highest redshift bins, the trend that prolateness decreases with time and mass remains invariant. Secondly, if at high redshift, the populations of galaxies were dominated by discy objects, we would be more likely to observe more small and edge-on discs rather than small and face-on ones, as the former have larger surface brightness. In fact what we observe is the existence of elongated galaxies in the high-redshift bins. This would lead to the conclusion that the real curved boundaries are even more pronounced than what we observed in the highest redshift bins of Fig. 2. Therefore, no matter whether we take the incompleteness in the highest redshift bins into consideration, the qualitative conclusion that these bins are dominated by elongated objects still holds, although quantitatively the actual fractions of elongated galaxies may change.

Dust attenuation may also complicate the situation. As Padilla & Strauss (2008) pointed out, the existence of dust may affect the detectability of disc galaxies in certain orientations. In the calculation of the apparent b/a–$\log a$ distribution of a galaxy, we assume that the galaxy is viewed from every direction in 4π solid space with equal probability. But, due to the fact that the light from stars in a disc galaxy is absorbed more significantly when it is viewed edge-on, some galaxies may drop out of the detection limit when viewed in this direction. Therefore the true distribution will deviate from the one calculated in this work.

7 CONCLUSION

We have found that the shapes of the star-forming galaxies in CANDELS are correlated with their sizes, in the sense that smaller galaxies are intrinsically rounder. Motivated by this insight, we expanded the previous work by van der Wel et al. (2014) by analysing the projected b/a–$\log a$ distributions of the CANDELS star-forming galaxies with $0.5 < z < 2.5$ and $9 < \log(M_*/\mathrm{M}_\odot) < 10.5$ in a grid of redshift and mass bins, assuming that the shapes of the three-dimensional light distributions of galaxies can be approximated by uniform triaxial ellipsoids, and the size and shape parameters of galaxies $(E, T, \gamma = \log \bar{a})$ has a multivariate normal distribution. By doing this modelling we give the fractions
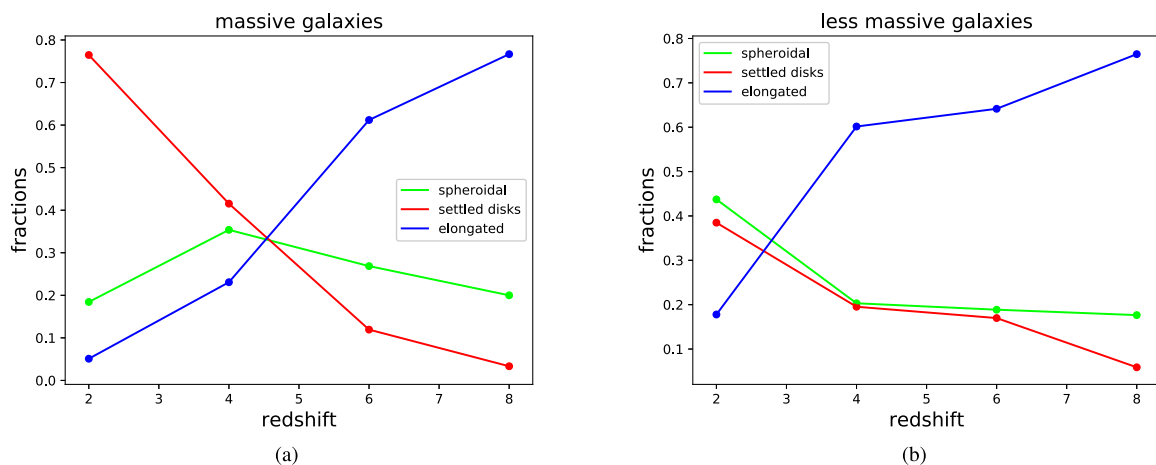
Figure 19. Panel (a): The time evolution of the fractions of three different shapes of the VELA galaxies as defined in Fig. 18, with only the more massive galaxies included. Panel (b): The same evolution but for the less massive VELA galaxies.

of elongated, discy, and spheroidal galaxies in each redshift and mass bin. Based on these fractions we find that galaxies tend to be prolate at low mass and high redshift, and discy at high mass and low redshift, which means galaxies evolve from prolate to discy. This transition tends to occur in a characteristic mass range, which tends to decline in time. Qualitatively our findings, summarized in Fig. 13, are in line with those of van der Wel et al. (2014). But quantitatively we find more prolate and/or spheroidal galaxies than they did, due to the existence of a new correlation between the (intrinsic or projected) shapes and the sizes of galaxies, in the sense that smaller galaxies are systematically rounder. We also verify that such a correlation is not an artificial effect induced by selection bias in the CANDELS pipelines. The fact that we find more discy objects in more massive and lower redshift bins is also consistent with the findings by Jiang et al. (2018), who also effectively considered the correlation between the galaxies' intrinsic shapes and their sizes. But we note that when comparing small and large star-forming galaxies in the same redshift-mass bins, they argued that the latter are more likely to have disc-like components flattened by rotation. This is not fully consistent with our finding, which is that larger galaxies could be more discy *or more elongated*. This is due to the fact that Jiang et al. (2018) did not take into account the fact that elongated galaxies could also have large ellipticities, and thus not being able to cover the case in which some of the larger star-forming galaxies are in fact elongated, instead of discy.

We compared the results of the modelling of CANDELS data with the VELA simulation (Ceverino et al. 2014; Zolotov et al. 2015) data as 'observed' in two-dimensional projection through dust, mimicking the observational features of the CANDELS observations. By comparing multiband images from both data sets, we argue that it is not feasible to tell whether a galaxy is an edge-on disc or an elongated object from direct images due to their similar projected morphologies. Secondly, we demonstrate that in high-redshift and low-mass bins, the *b*/*a*–log *a* distributions are qualitatively consistent with a prolate-dominated galaxy population, by comparing CANDELS data in such bins with the same distributions of the prolate galaxies in the VELA simulation. Thirdly, we investigate the time evolution of the fractions of different shapes of galaxies in the VELA simulations and find the same trend with time and mass as found in the CANDELS data. This finding further confirms the picture proposed by Kassin et al. (2012) and Simons et al. (2016, 2017), based on kinematic data of real observed galaxies,

and Kassin et al. (2014), Ceverino et al. (2015), Tomassetti et al. (2016), and Ceverino et al. (2017) based on hydrodynamic models, that the rotational support in galaxies grows with time, which is a process that starts earlier in more massive galaxies. Our results are also consistent with the predictions from the VELA simulations (Ceverino et al. 2015; Tomassetti et al. 2016) that the transition of shape occurs in a characteristic mass range, where galaxies tend to undergo a process of wet compaction to a BN, and make a transition from being dark matter dominated to baryon dominated. See also Huertas-Company et al. (2018) and Dekel et al. (in preparation).

How galaxies achieve their final structure is one of the most basic aspects of galaxy evolution. The emerging story – coming from both data and theory – seems to be that the process is gradual but is more advanced in massive galaxies at a given redshift. In this sense, the process of structural evolution is coming to resemble the cycle of star formation and quenching, which is also more advanced in massive galaxies at each *z*. This latter phenomenon has come to be known as 'downsizing' (Cowie et al. 1996). Drawing the parallel with star formation, Kassin et al. (2012) coined the term 'kinematic downsizing' to describe their finding that massive galaxies at any given redshift are more settled. It will be interesting and instructive to compare and contrast the phenomena of structural evolution and the star formation life cycle going forward to see if their trajectories are in fact parallel and how their underlying physics compares.

Using the results of such modellings, we are able to give the probabilities of a galaxy's being elongated, discy, or spheroidal, as a function of its redshift, mass, *b*/*a*, and log *a*. This can be used to facilitate the target selections for kinematics or spectroscopic observations of the elongated galaxies in the future.

For readers' convenience we also summarize the availability of the data and results involved in this paper here. The CANDELS catalogue can be accessed via http://arcoiris.ucsc.edu//Rainbow_navigator_public/. The ETa modelling results given by this work, including the comparisons between the data and model, and the probability maps (see Section 5.2) can be found at https://sites.google.com/site/zhw11387/Home/research.

REFERENCES

Allgood B., Flores R. A., Primack J. R., Kravtsov A. V., Wechsler R. H., Faltenbacher A., Bullock J. S., 2006, MNRAS, 367, 1781
Barro G. et al., 2011, ApJS, 193, 13
Barro G. et al., 2013, ApJ, 765, 104
Ceverino D., Klypin A., Klimek E. S., Trujillo-Gomez S., Churchill C. W., Primack J., Dekel A., 2014, MNRAS, 442, 1545
Ceverino D., Primack J., Dekel A., 2015, MNRAS, 453, 408
Ceverino D., Primack J., Dekel A., Kassin S. A., 2017, MNRAS, 467, 2664
Chang Y.-Y. et al., 2013, ApJ, 773, 149
Cowie L. L., Songaila A., Hu E. M., Cohen J. G., 1996, AJ, 112, 839
Dalcanton J. J., Bernstein R. A., 2002, AJ, 124, 1328
Elmegreen D. M., Elmegreen B. G., Rubin D. S., Schaffer M. A., 2005, ApJ, 631, 85
Fang J. J., 2015, PhD thesis, University of California
Fang J. J. et al., 2018, ApJ, 858, 100
Galametz A. et al., 2013, ApJS, 206, 10
Grogin N. A. et al., 2011, ApJS, 197, 35
Guo Y. et al., 2013, ApJS, 207, 24
Holden B. P., van der Wel A., Rix H.-W., Franx M., 2012, ApJ, 749, 96
Huertas-Company M. et al., 2018, ApJ, 858, 114
Jiang D. et al., 2018, ApJ, 854, 70
Jonsson P., 2006, MNRAS, 372, 2
Jonsson P., Primack J. R., 2010, New Astron, 15, 509
Jonsson P., Groves B. A., Cox T. J., 2010, MNRAS, 403, 17
Kassin S. A. et al., 2012, ApJ, 758, 106
Kassin S. A., Brooks A., Governato F., Weiner B. J., Gardner J. P., 2014, ApJ, 790, 89
Koekemoer A. M. et al., 2011, ApJS, 197, 36
Law D. R., Steidel C. C., Shapley A. E., Nagy S. R., Reddy N. A., Erb D. K., 2012, ApJ, 745, 85
Nayyeri H. et al., 2017, ApJS, 228, 7
Padilla N. D., Strauss M. A., 2008, MNRAS, 388, 1321
Peng C. Y., Ho L. C., Impey C. D., Rix H.-W., 2010, AJ, 139, 2097
Ravindranath S. et al., 2006, ApJ, 652, 963
Santini P. et al., 2015, ApJ, 801, 97
Simons R. C. et al., 2016, ApJ, 830, 14
Simons R. C. et al., 2017, ApJ, 843, 46
Snyder G. F., Lotz J., Moody C., Peth M., Freeman P., Ceverino D., Primack J., Dekel A., 2015, MNRAS, 451, 4290
Stefanon M. et al., 2017, ApJS, 229, 32
Tacchella S., Dekel A., Carollo C. M., Ceverino D., DeGraf C., Lapiner S., Mandelker N., Primack J. R., 2016a, MNRAS, 457, 2790
Tacchella S., Dekel A., Carollo C. M., Ceverino D., DeGraf C., Lapiner S., Mandelker N., Primack J. R., 2016b, MNRAS, 458, 242
Tomassetti M. et al., 2016, MNRAS, 458, 4477
Tuccillo D., Huertas-Company M., Decencière E., Velasco-Forero S., Sánchez H. D., Dimauro P., 2018, MNRAS, 475, 894
van der Wel A. et al., 2012, ApJS, 203, 24
van der Wel A. et al., 2014, ApJ, 792, L6
Williams R. J., Quadri R. F., Franx M., van Dokkum P., Labbé I., 2009, ApJ, 691, 1879
Wuyts S. et al., 2007, ApJ, 655, 51
Zolotov A. et al., 2015, MNRAS, 450, 2327

SUPPORTING INFORMATION

Supplementary data are available at *MNRAS* online.

Please note: Oxford University Press is not responsible for the content or functionality of any supporting materials supplied by the authors. Any queries (other than missing material) should be directed to the corresponding author for the article.

APPENDIX A: TESTS OF POTENTIAL SELECTION EFFECTS IN THE CANDELS PIPELINE

In Section 2 we claimed that the curved boundary and the lack of objects in the upper right corner of each $b/a - \log a$ panel is not due to the selection effects induced by the detection scheme in CANDELS or the measurement process in GALFIT. Here we describe how a two-step experiment using SEXTRACTOR and GALFIT (Peng et al. 2010) establishes this by mocking up the procedures implemented in the pipeline.

We first explain the possible reasons why these two features could be induced by the selection bias in source detection and measurements. As pointed out in Section 3, the probability distribution of an elongated galaxy in b/a–$\log a$ space is a curved ridgeline from lower right to upper left in this space and is thus naturally compatible with these two features; on the other hand, the distribution of a spheroidal galaxy is localized at a high b/a value, and thus the detectability of such an object and the accuracy of the measurements would not change much as the viewing direction varies. Therefore, it is natural to conclude that the selection bias of the pipeline, if any, would affect the discy populations in the sample most significantly.

Bearing this in mind, it is easy to imagine how the two features in the observed distribution can be explained by a selection bias on discy objects:

(1) The lack of objects in the upper right corner may be due to the fact that, when a disc galaxy is viewed face-on, due to the smaller path-length through the galaxy, its surface brightness is lower than when it is viewed edge-on. This decrease of surface brightness may make some of the fainter disc galaxies drop out of the sample because they are too faint to be detected when viewed face-on. But their edge-on counterparts are still included in the sample due to relatively higher surface brightness. Thus this kind of discrepancy of different surface brightness at different b/a values could cause the lack of objects in the upper right corner.

(2) The curved lower boundary essentially tells us that there is minimum shortest main axis length of galaxies which is not
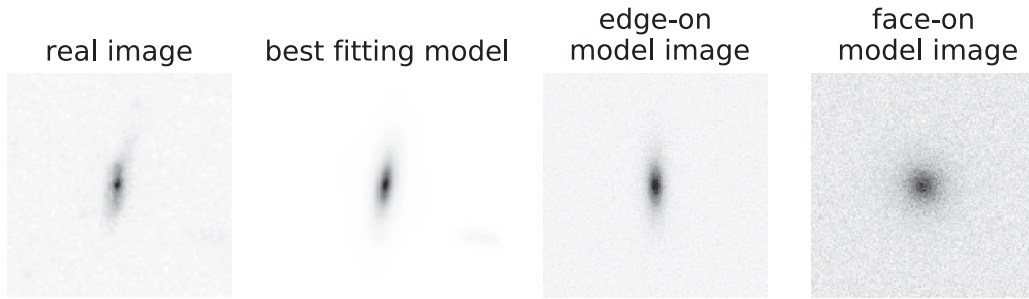
Figure A1. Illustration of mock image generation. The first panel from the left is the cut-out stamp from a CANDELS multidrizzled image. The second panel is the best-fitting Sérsic model obtained by van der Wel et al. (2012). The third panel is the edge-on mock image generated using the formalisms from van de Ven & van der Wel (in preparation), based on the assumption that the galaxy is discy, and with PSF and realistic sky background noise taken into account. The fourth panel is generated in the identical way to the third one, except for being viewed face-on.

proportional to the semimajor axis, and therefore we do not observe many small and highly flattened objects. But in principle this may simply be an artificial effect induced by either the detection or the measurement scheme. First, when a small galaxy gets more and more flattened (and correspondingly fainter and fainter, which can be seen from the visual inspection of the images), its image gets more and more vulnerable to being lost in sky noise. Given the dual-mode SEXTRACTOR detection strategy (Galametz et al. 2013), it is possible that such an object escapes detection in the cold mode and ends up being separated into multiple objects in the hot mode. In this case this galaxy would be regarded as multiple objects, so naturally we cannot get small and also very flattened galaxies in the catalogue. Another possible cause lies in the measurement phase. As we know all the images are pixelated, and thus the fact that we did not observe such small and flattened objects may be due to the fact that these objects have a too small semiminor axis which is significantly smaller than 1 pixel, so that all the measurements on such objects are not usable.

Based on these hypotheses for the origin of these two features, we do the following experiments:

(1) To investigate the origin of the lack of objects in the upper right corner, we pick out large and thin edge-on disc galaxies from the catalogue, calculate their corresponding face-on light profiles using the formalisms introduced by van de Ven & van der Wel (in preparation), add realistic sky background noise, feed these mock images into SEXTRACTOR and GALFIT, and see whether we get fewer objects detected or measured accurately. The set-ups of SEXTRACTOR and GALFIT are identical to those introduced in Galametz et al. (2013) and van der Wel et al. (2012).

(2) To investigate the origin of the curved lower boundary, we pick out small and round galaxies and calculate their edge-on light profiles based on the assumption that they are small and thin discs. After that all the procedures are the same as with experiment (1).

Fig. A1 shows an example of such a deprojected Sérsic modelling. From left to right, the figure shows the original image from CANDELS, the best-fitting model from GALFIT, the edge-on model image, and the face-on model image. By doing such experiments, we found that large and round (small and thin) discs do have lower detectability than their large and thin (small and round) counterparts, but only roughly by ∼20 per cent, which is far from sufficient to account for the lack of objects at either the upper right or the lower left corner. On the other hand, when we view the small model disc galaxies edge-on, their *b/a* can still be measured accurately. Therefore we arrive at the conclusion that neither of these two

features is caused by the selection bias intrinsic to the CANDELS pipeline.

APPENDIX B: SINGLE-SÉRSIC MODELLING OF GALAXIES

Throughout this work we have been modelling the galaxies as solid triaxial ellipsoids (ellipsoidal modelling), with projected structural parameters measured directly from their two-dimensional projections. In fact there is a potential improvement of such a kind of modelling, which will be introduced in this section.

According to van de Ven & van der Wel (in preparation), every two-dimensional Sérsic profile can be produced by projecting a three-dimensional profile (hereafter 3D profile) in a certain direction. Thus it is feasible for us to model every galaxy as such a 3D profile. For different galaxies, the scale lengths and the shapes of the 3D profiles differ. By the projection of each of these galaxies randomly in many directions we get multiple images, which will be fed into GALFIT to measure their structural parameters. As a result, we get a *b/a*–log *a* distribution measured by GALFIT, instead of a simple geometrical calculation, and we can use these distributions in the modelling instead.

In principle this Sérsic modelling method is more realistic than the solid ellipsoid method, in the sense that first it assumes a galaxy can be well approximated by a single two-dimensional Sérsic profile, which, although still simplified, is much closer to the reality than the ellipsoidal modelling, in the sense that the galaxies are transparent in this model. Secondly the *b/a* and *a* come from GALFIT, which is the exact way of getting these parameters in real observations. However, such a method has the unfortunate drawback that to generate as many element distributions as we did with the solid modelling, the measurements of GALFIT would take more computer time than is available for us at the moment. Another possibility is to make use of a deep learning technique, e.g. Tuccillo et al. (2018), which is demonstrated to be much faster than GALFIT, to carry out massive measurements like this. But it remains to be evaluated whether such deep learning measurements are statistically consistent with what one gets from GALFIT.

As is seen in Fig. 5, the *b/a*–log *a* distributions generated by the two modelling methods are qualitatively similar in their shapes, but the magnitudes of scatter differ. This may be due to the fact that the measurement uncertainties obtained by van der Wel et al. (2012) incorporate random measurement uncertainties by comparing the measurements for the same objects in different data sets, which is not implemented in our Sérsic modelling. But the overall similarities between the shapes of the distributions from the two different

modellings convinces us that the main conclusions in this work will not change qualitatively if we adopt the more realistic Sérsic modelling instead.

APPENDIX C: THE EFFECT OF EMPIRICAL CORRECTIONS TO THE b/a–LOG a DISTRIBUTIONS

As was pointed out in Section 4.1, the effect of dust on the measurements of the semimajor axis a of edge-on discy galaxies ought to change the shape of the distributions, producing small tails in the lower right corner. We tried to make some empirical corrections to this in some of the redshift-mass bins. From Fig. 2 we see that the only two bins where such tails show up significantly are $0.5 < z < 1.0$ with $9.5 < \log(M_*/M_\odot) < 10.0$ and $10.0 < \log(M_*/M_\odot) < 10.5$. In these two bins we assume the lower right tails are dominated by discy galaxies that have been moved to larger a and smaller b/a due to central dust attenuation. According to Fig. 5, we know that the b/a–$\log a$ distribution of a disc galaxy should possess a vertical boundary; thus we move the data points leftward in the tails so that the corrected boundary is roughly a vertical line. In the correction we assume the semiminor axis b of the galaxy is invariant; therefore a correction of a naturally leads to a correction of b/a. As a result, the data points are moved diagonally upward instead of horizontally. Fig. C1 compares the corrected and uncorrected distributions of the galaxies with $0.5 < z < 1.0$ and $10 < \log(M_*/M_\odot) < 10.5$ (i.e. the late-discy bin).

We fed the corrected distribution to our modelling code to see whether the results changed significantly. The comparison between the best-fitting parameters and the fractions of the different shapes is listed in Table C1. From the comparison we can see that we find 6.8 per cent (18.3 per cent) more discy galaxies in the corrected distribution in the $0.5 < z < 1$ and $9.5 < \log(M_*/M_\odot) < 10$ ($10 < \log(M_*/M_\odot) < 10.5$) bin, which is expected because the corrected b/a–$\log a$ has a roughly vertical boundary, characteristic of a discy population. But qualitatively our picture that the oblateness increases with time and mass is not only not damaged by this correction but instead strengthened by the larger fractions of discy galaxies found in the low-redshift Universe. Therefore we argue that such empirical corrections do not affect the conclusions of this work.
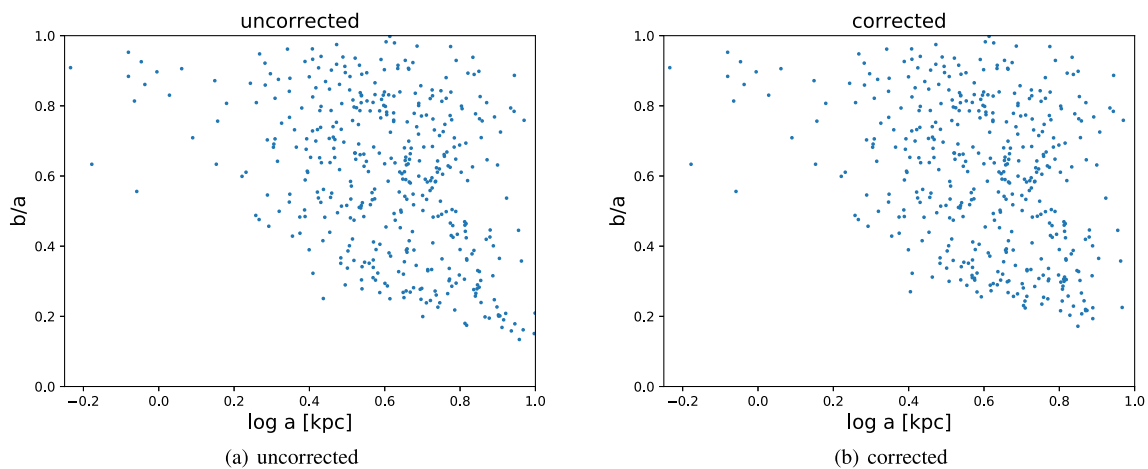
(a) uncorrected

(b) corrected

Figure C1. The uncorrected and corrected b/a–$\log a$ distribution of the galaxies with $0.5 < z < 1.0$ and $10 < \log(M_*/M_\odot) < 10.5$ (i.e. the late-discy bin). Left-hand panel: the uncorrected distribution. Right-hand panel: the corrected distribution.

Table C1. Best-fitting model parameters and fractions of the three shapes of each redshift-mass bin.

Redshift	$\log(M_*/M_\odot)$	correction	$\bar{E}$	$\bar{T}$	$\bar{\gamma}$	σ_{EE}	σ_{TT}	$\sigma_{\gamma\gamma}$	$\sigma_{E\gamma}$	$f_{\text{elongated}}$	f_{discy}	$f_{\text{spheroidal}}$	N_{obs}
0.75	9.75	no	0.745	0.156	0.574	0.008	0.658	0.043	0.016	0.324	0.561	0.115	1024
0.75	9.75	yes	0.747	0.174	0.567	0.004	0.627	0.039	0.010	0.347	0.599	0.053	1024
0.75	10.25	no	0.728	0.166	0.680	0.035	0.039	0.062	0.038	0.013	0.678	0.309	426
0.75	10.25	yes	0.714	0.133	0.652	0.011	0.039	0.054	0.022	0.012	0.802	0.186	426

This paper has been typeset from a TeX/LaTeX file prepared by the author.